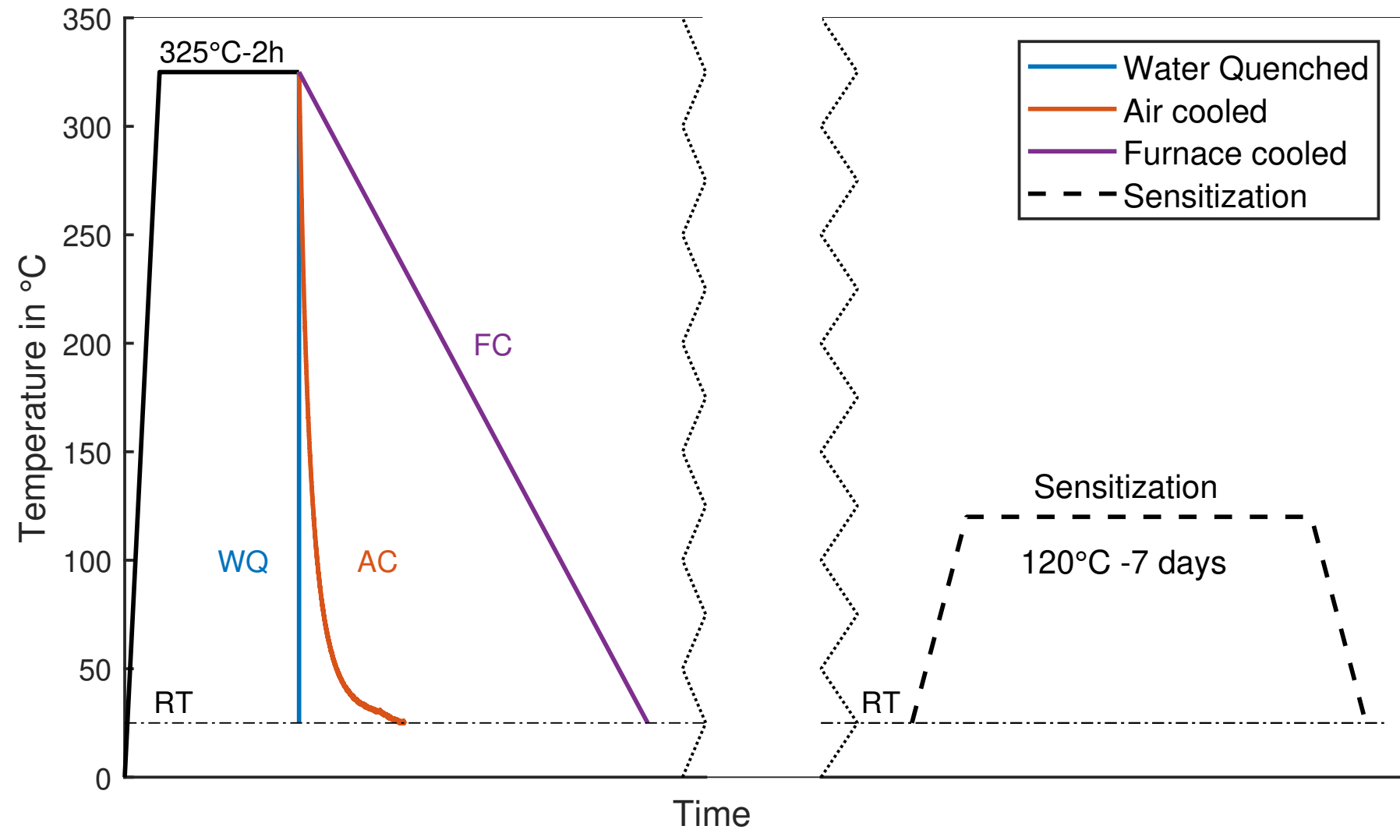


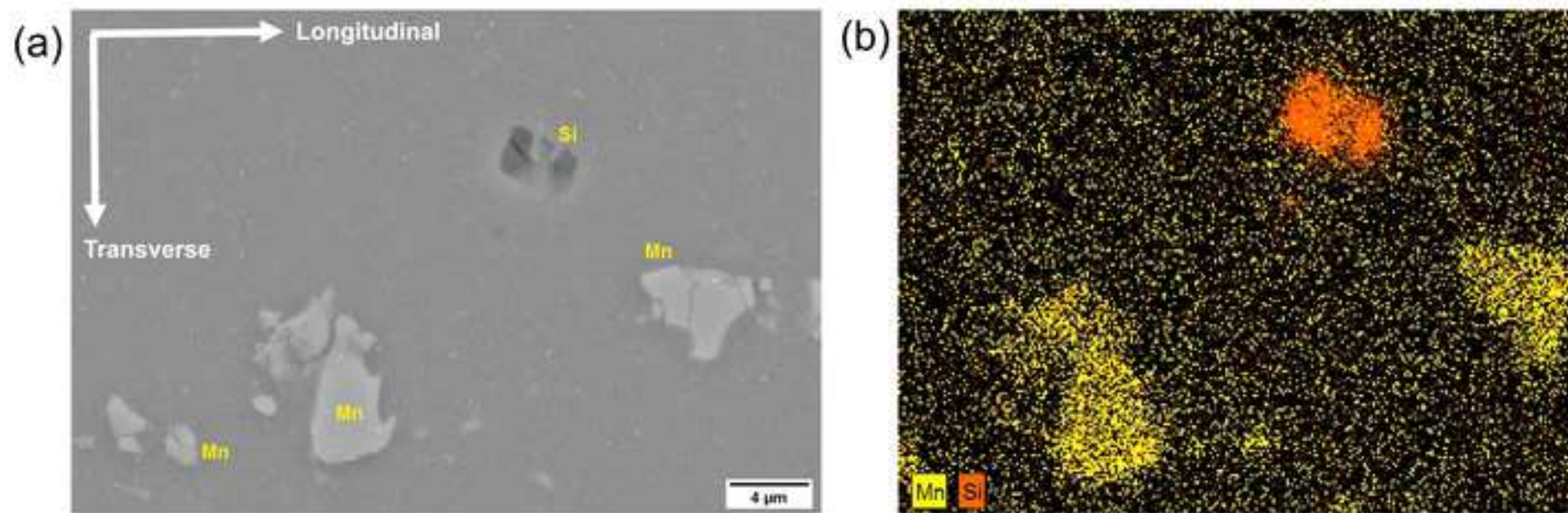
This item is the archived peer-reviewed author-version of:

Controlled precipitation in a new Al-Mg-Sc alloy for enhanced corrosion behavior while maintaining the mechanical performance

Reference:

Krishnamurthy Sanjay C., Arseenko Mariia, Kashiwar Ankush, Dufour Philippe, Marchal Yves, Delahaye Jocelyn, Idrissi Hosni, Pardoen Thomas, Mertens Anne, Simar Aude.- Controlled precipitation in a new Al-Mg-Sc alloy for enhanced corrosion behavior while maintaining the mechanical performance
Materials characterization - ISSN 1873-4189 - 200(2023), 112886
Full text (Publisher's DOI): <https://doi.org/10.1016/J.MATCHAR.2023.112886>
To cite this reference: <https://hdl.handle.net/10067/1955980151162165141>





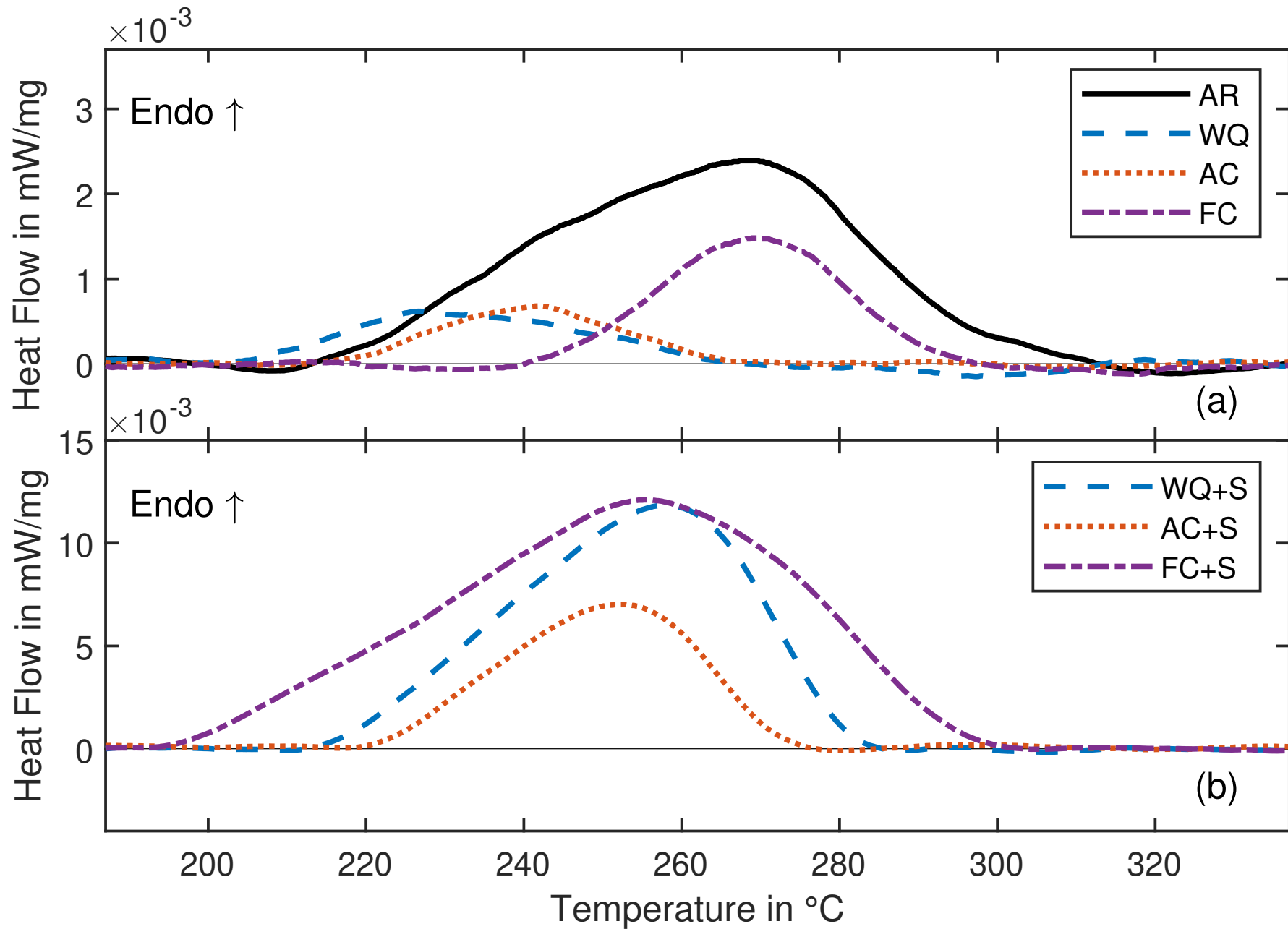
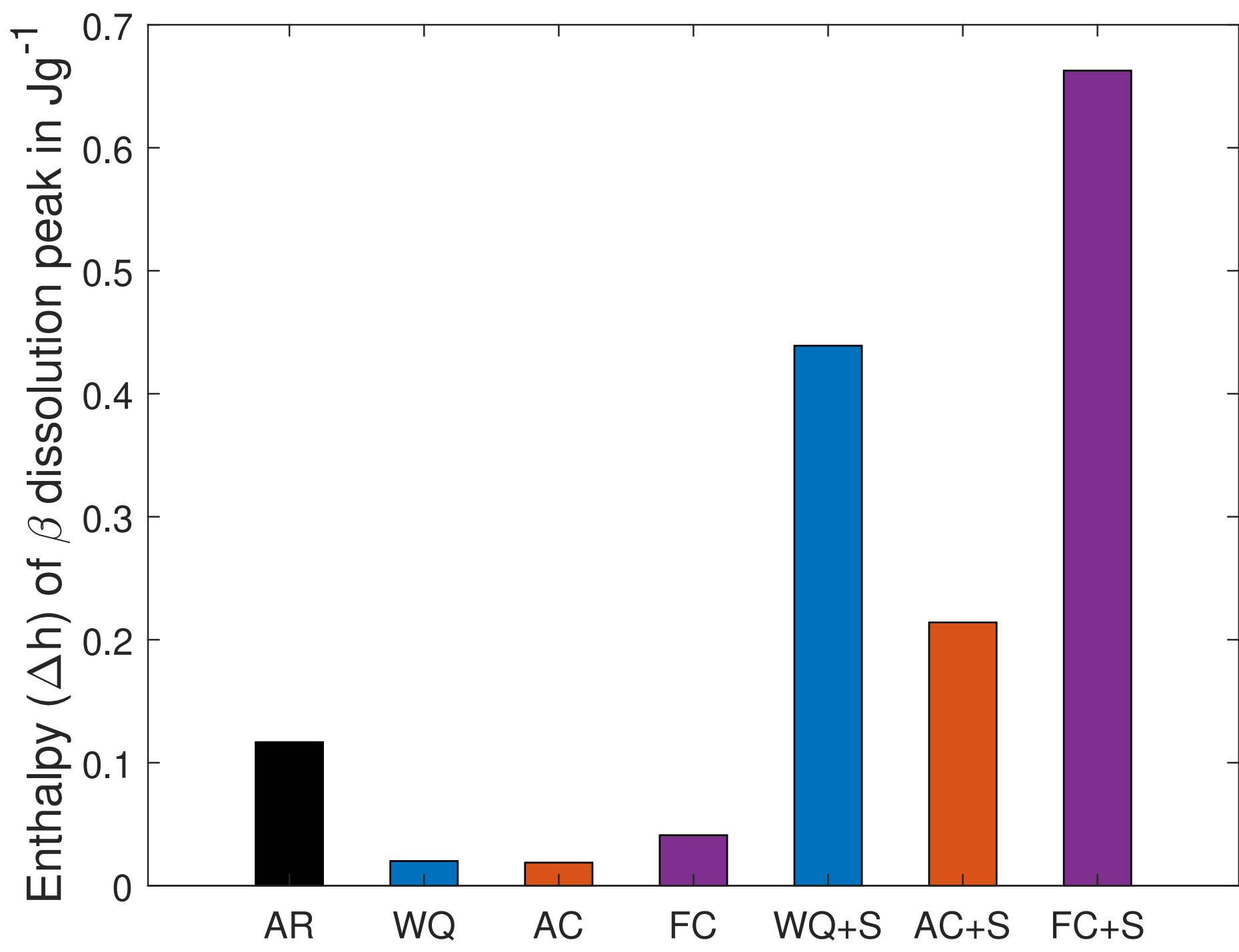
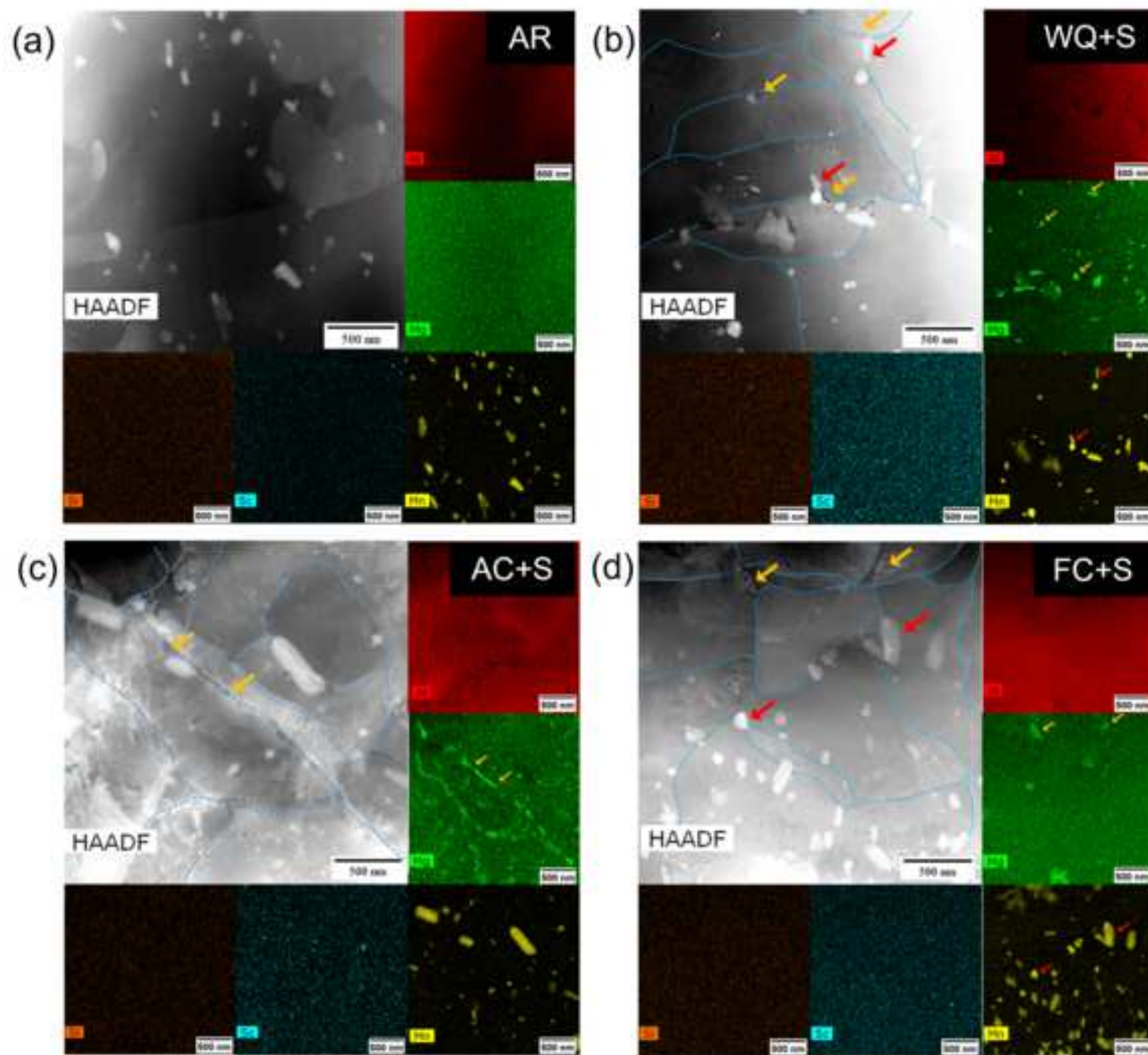
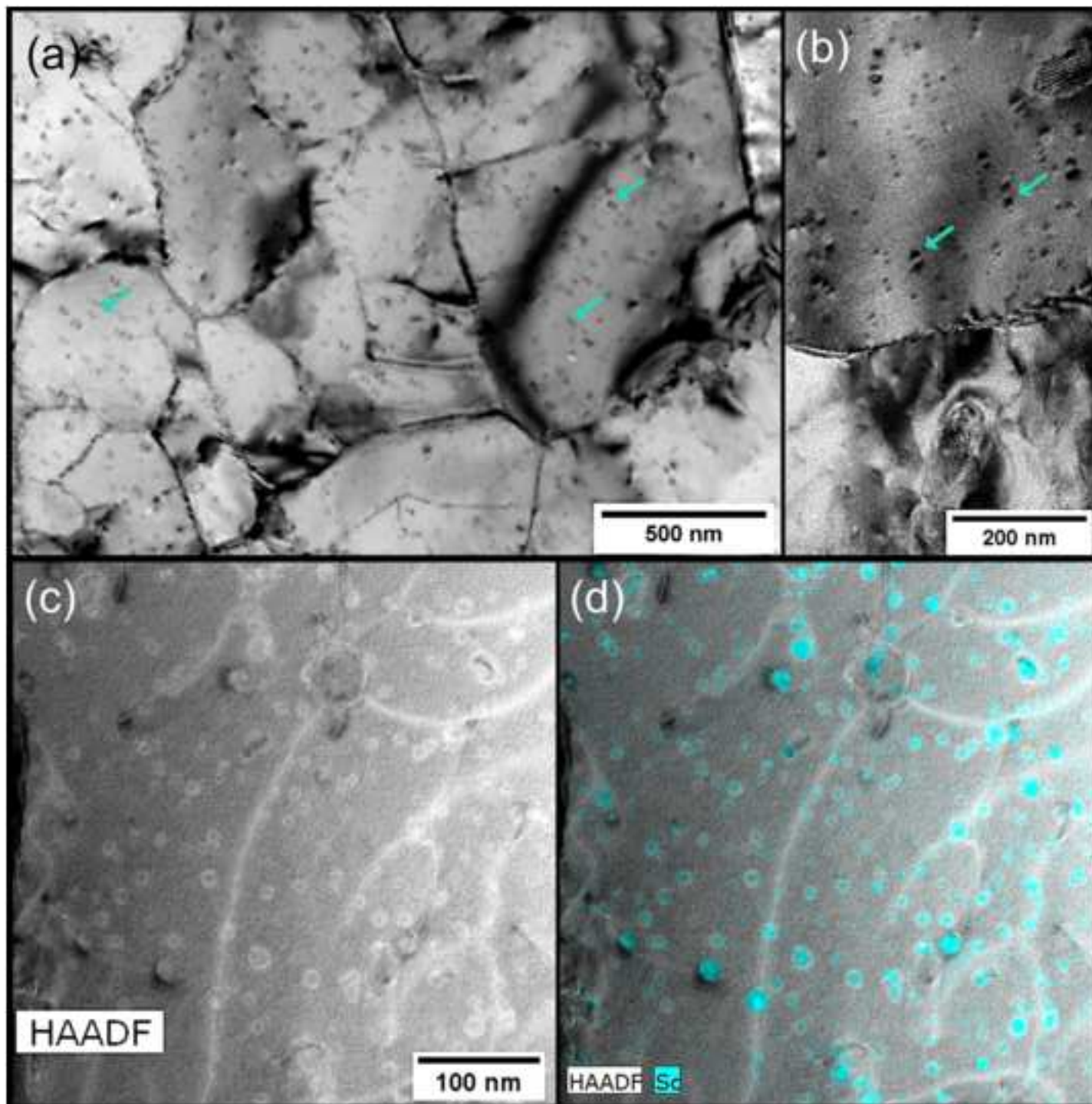
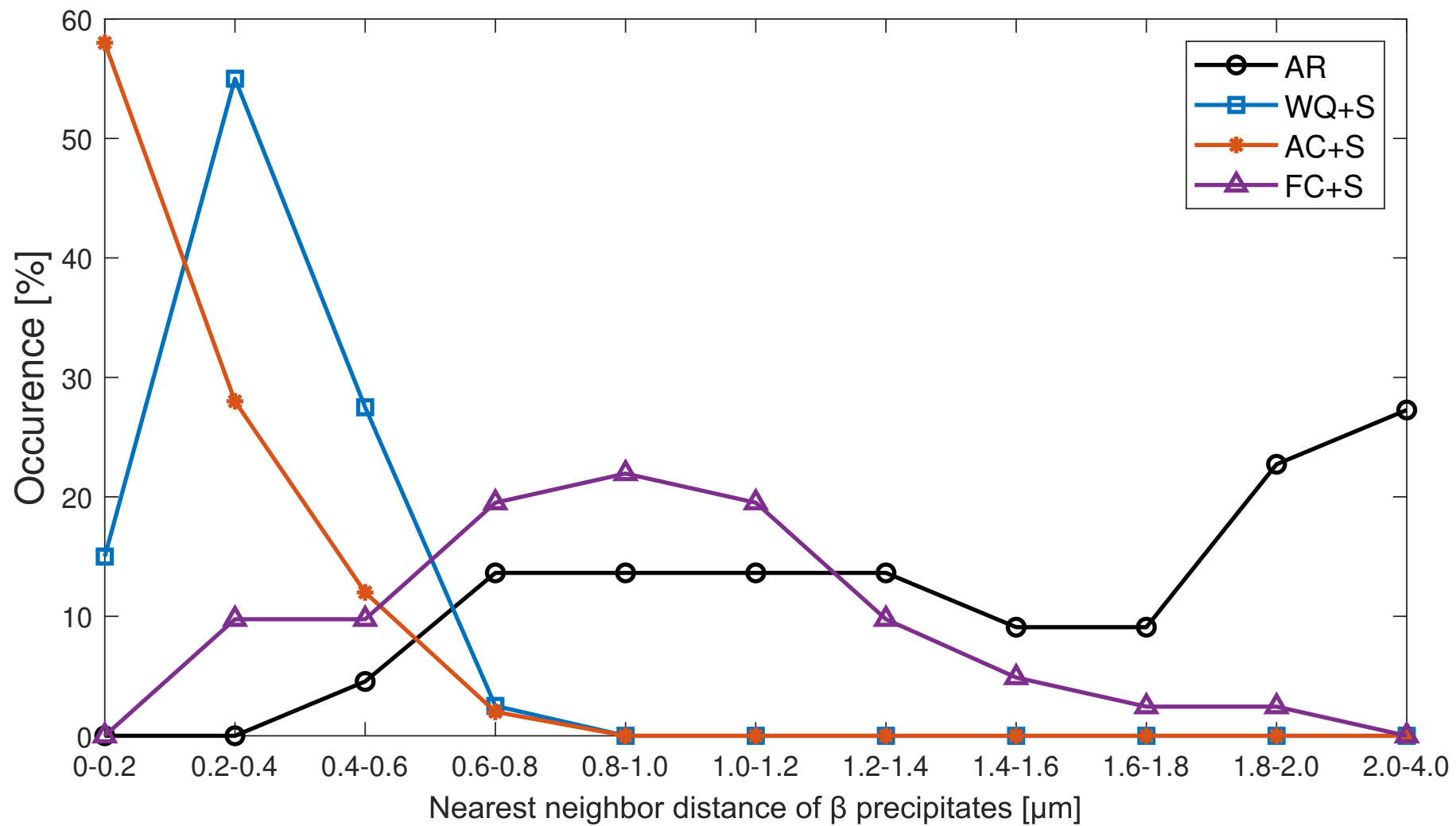


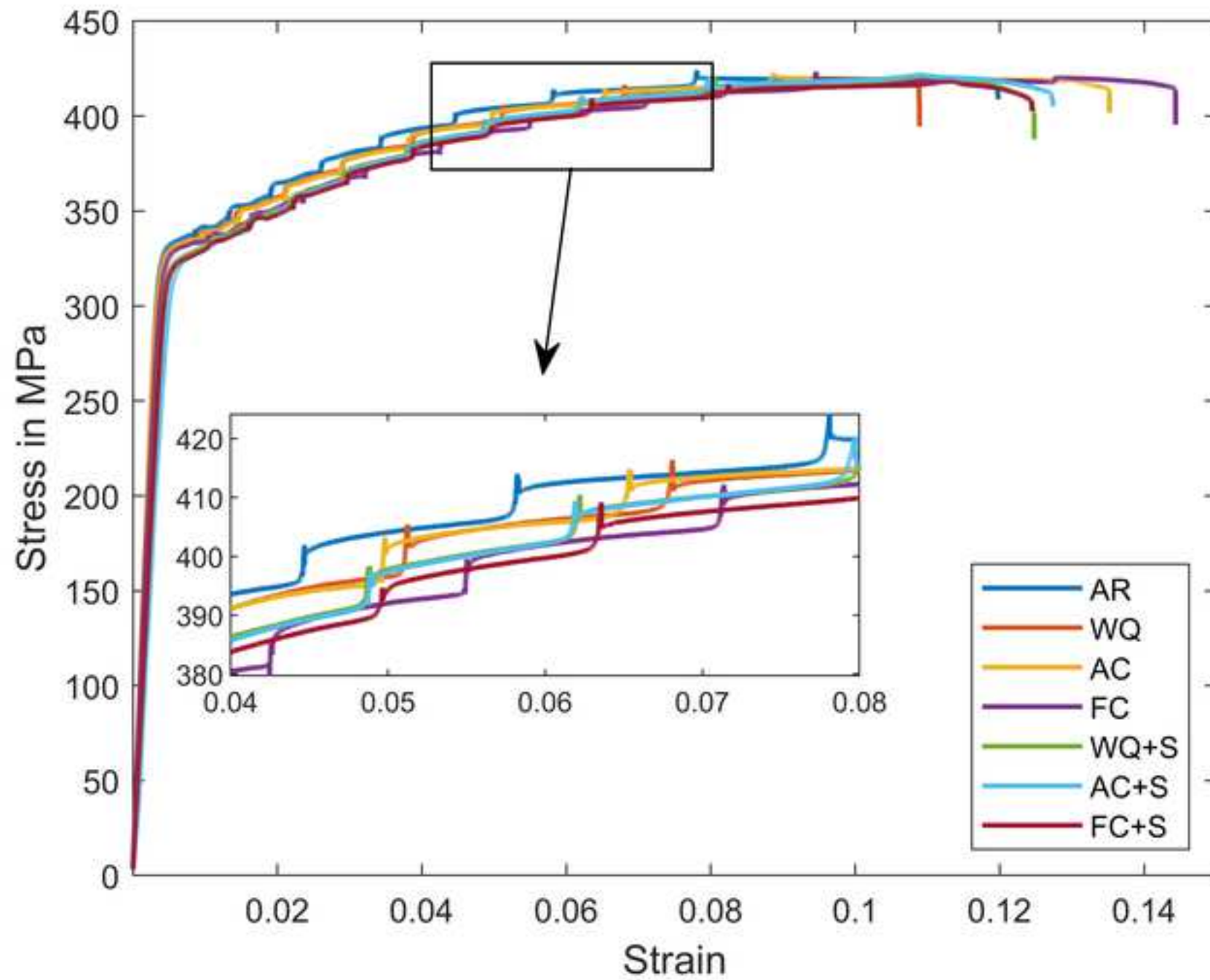
Figure 4

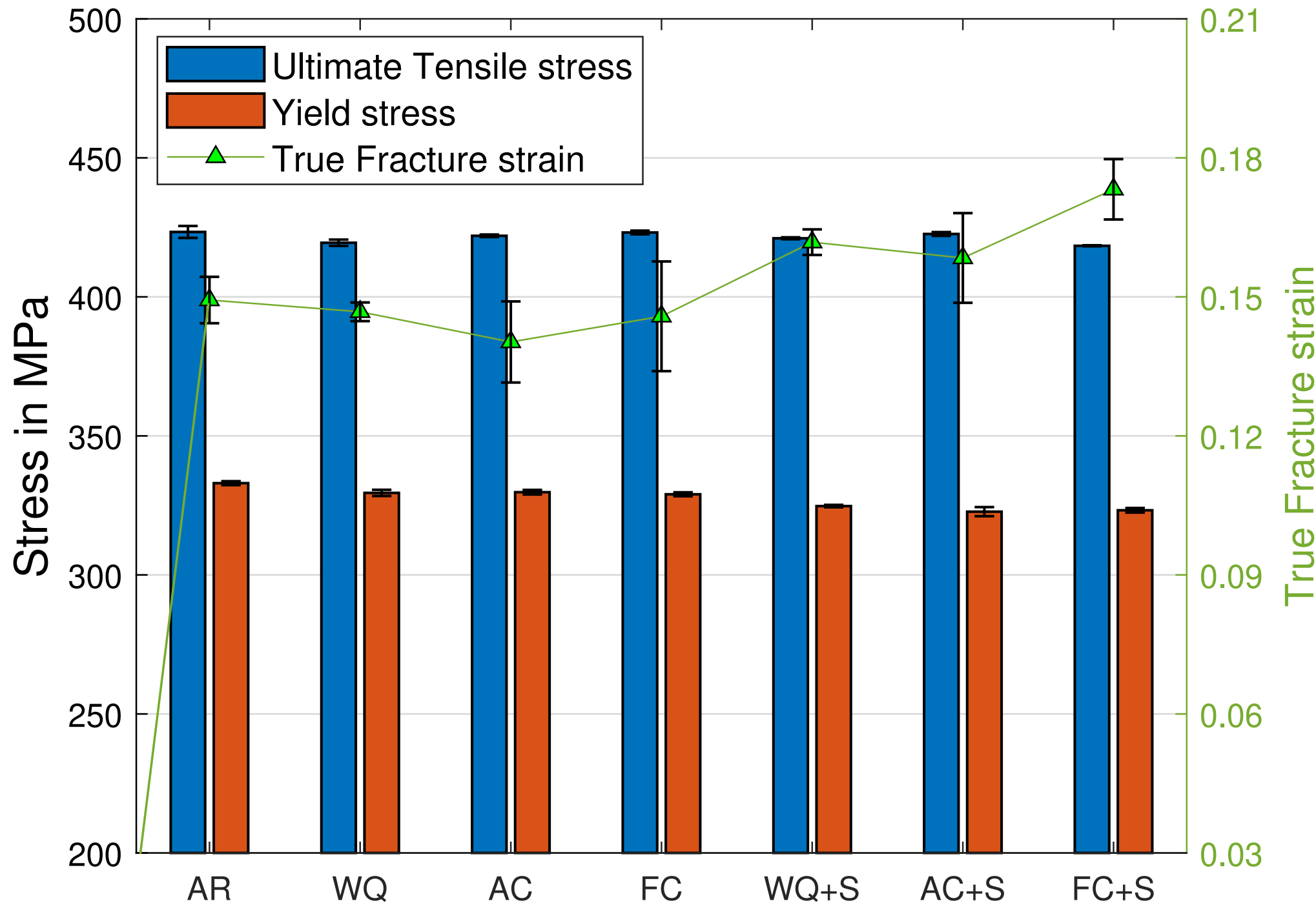


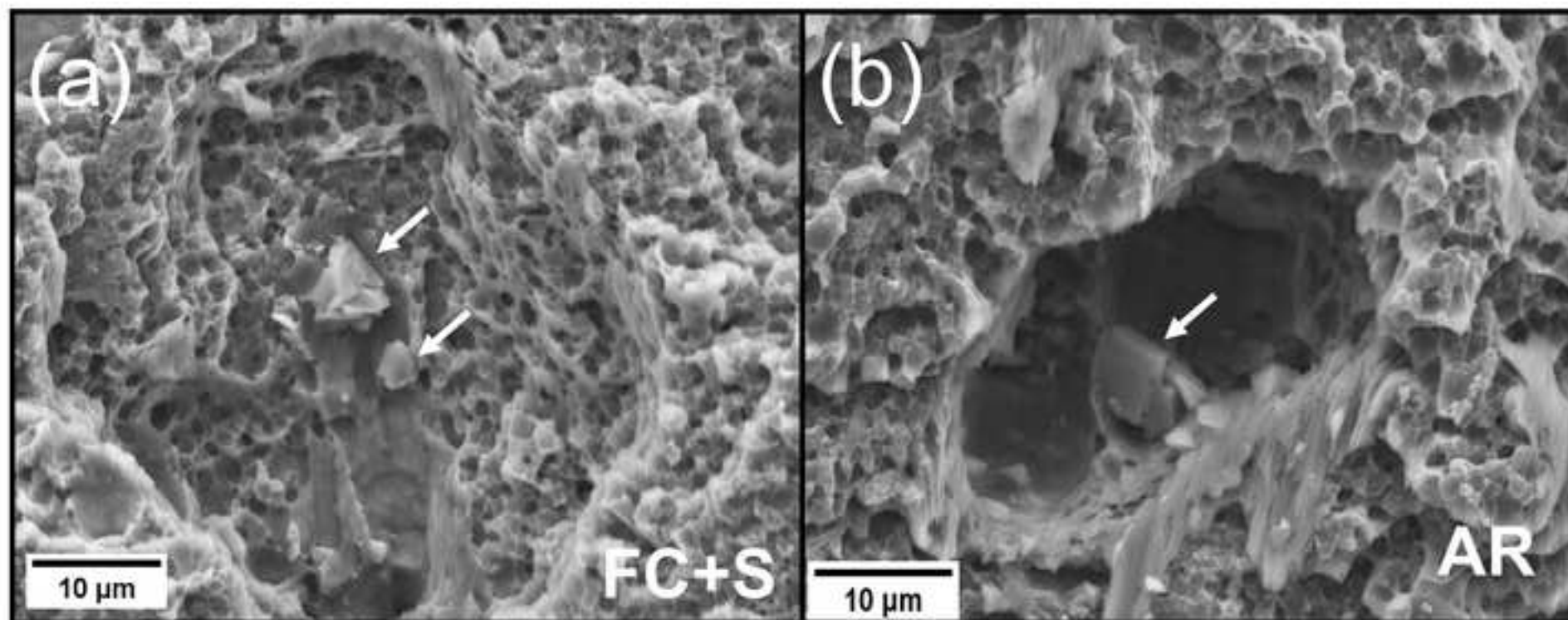


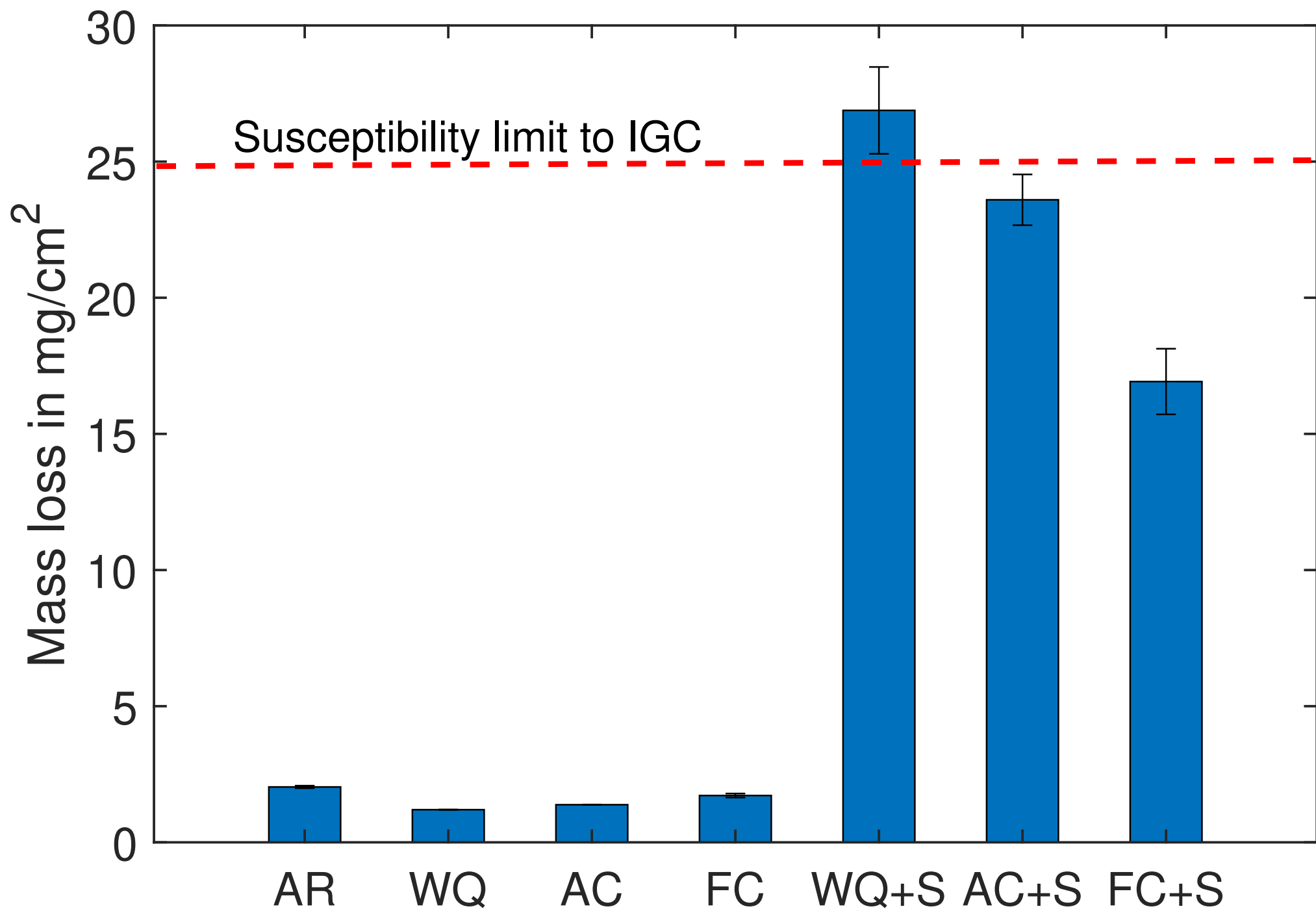


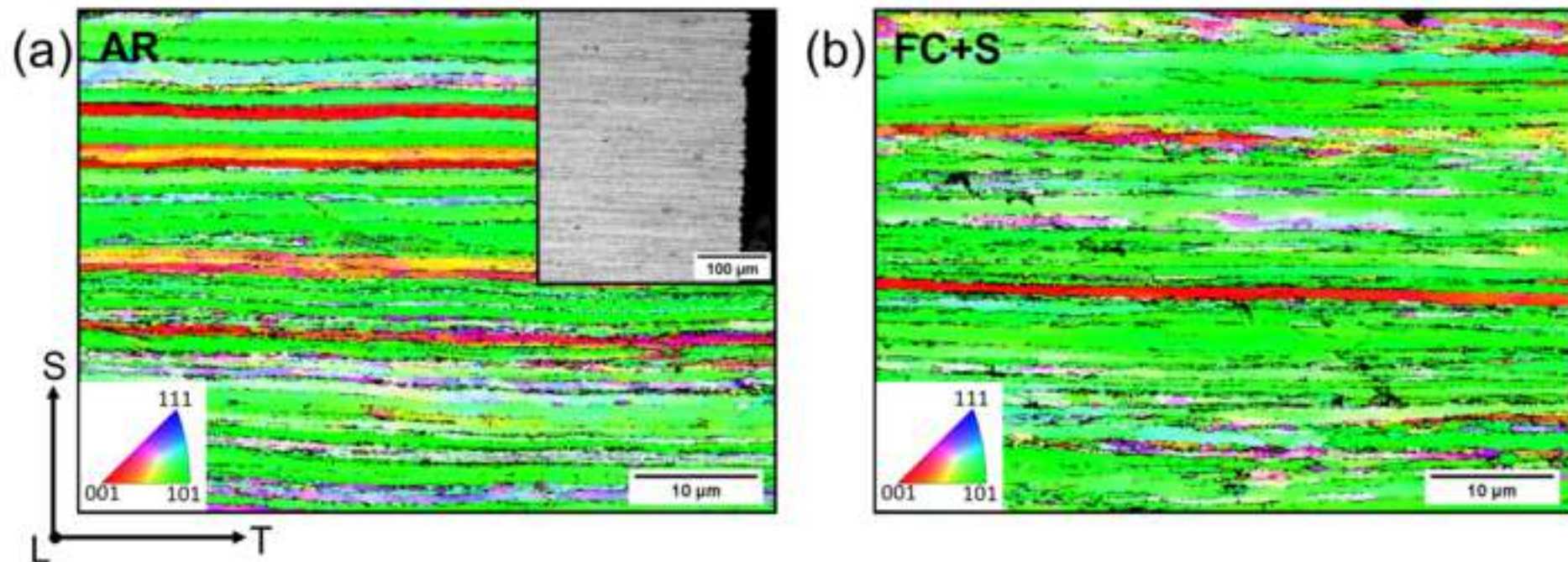


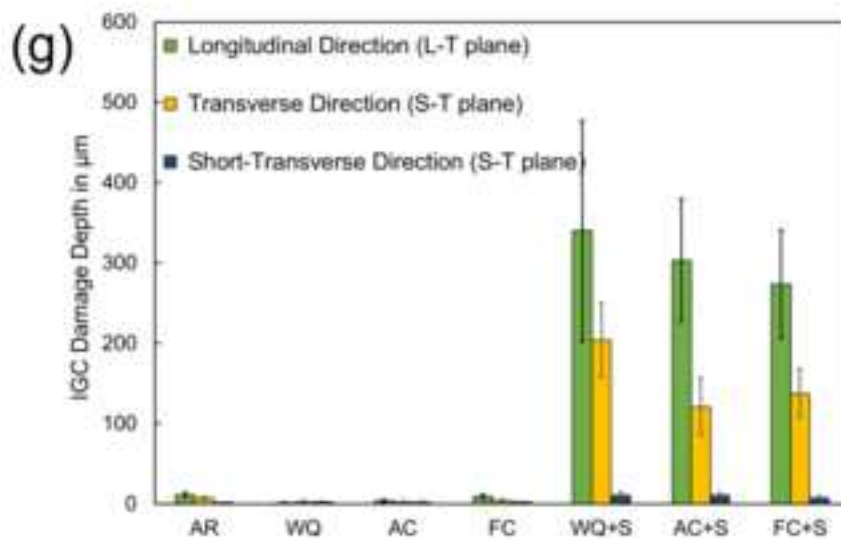
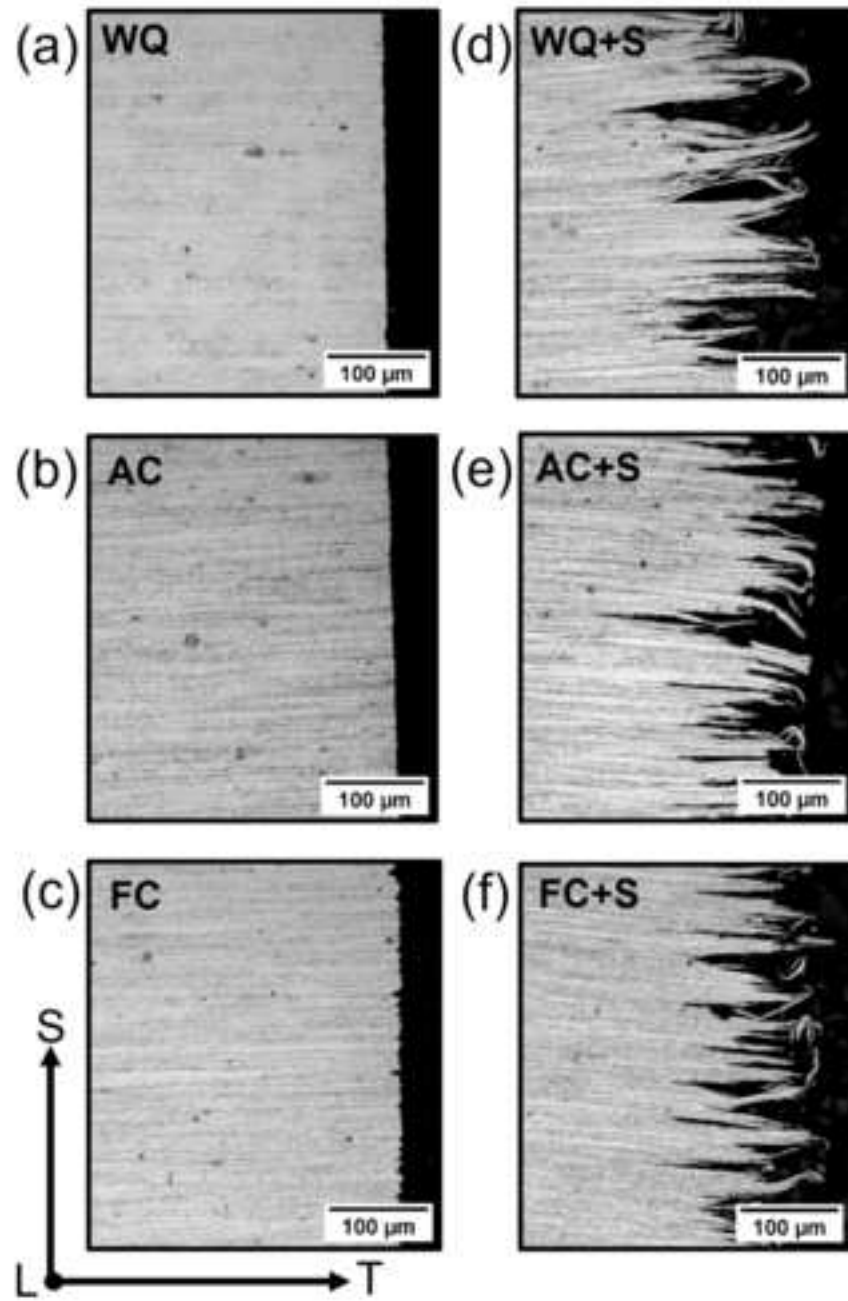












Highlights

- No effect of annealing and sensitization on mechanical property of 5028-H116 aluminium alloy.
- Slower cooling favors a better corrosion resistance during sensitization.
- β precipitates distribution influences significantly the corrosion resistance.

1 **Controlled precipitation in a new Al-Mg-Sc alloy for enhanced corrosion** 2 **behavior while maintaining the mechanical performance**

3 *Sanjay C Krishnamurthy*^a, *Mariia Arsenko*^a, *Ankush Kashiwar*^{a,b}, *Philippe Dufour*^c, *Yves Marchal*^c,
4 *Jocelyn Delahaye*^d, *Hosni Idrissi*^{a,b}, *Thomas Pardoën*^a, *Anne Mertens*^d and *Aude Simar*^{a,*}

5 ^a *Université catholique de Louvain, Institute of Mechanics, Materials and Civil Engineering (iMMC),*
6 *IMAP, Place Sainte Barbe 2, B-1348 Louvain-la-Neuve, Belgium*

7 ^b *Department of Physics, Electron Microscopy for Materials Science (EMAT), University of Antwerp,*
8 *Groenenborgerlaan 171, B-2020 Antwerpen, Belgium*

9 ^c *SONACA, Gosselies, Belgium*

10 ^d *Université de Liège, Aerospace and Mechanics Department, Metallic Materials Science, Allée de la*
11 *Découverte 13A, Quartier Polytech 1, B-4000, Liège, Belgium*

12 **Abstract** - The hot working of 5xxx series alloys with Mg ≥ 3.5 wt% is a concern due to the
13 precipitation of β (Al_3Mg_2) phase at grain boundaries favoring Inter Granular Corrosion (IGC).
14 The mechanical and corrosion properties of a new 5028-H116 Al-Mg-Sc alloy under various β
15 precipitates distribution is analyzed by imposing different cooling rates from the hot forming
16 temperature (i.e. 325 °C). The mechanical properties are maintained regardless of the heat
17 treatment. However, the **different nucleation sites and volume fractions of β precipitates for**
18 **different cooling rates** critically affect IGC. Controlled furnace cooling after the 325 °C heat
19 treatment is ideal in 5028-H116 alloy to reduce susceptibility to IGC after sensitization.

20 **Keywords:** Al-Mg-Sc alloy, Cooling rate, Inter granular Corrosion, Precipitation

22 **1. Introduction**

23 The application of 5xxx series aluminum alloy as structural components in aerospace industry
24 has gained renewed interest following the addition of scandium as micro-alloying element [1,
25 2]. The Al-Mg-Sc alloys have excellent toughness and damage tolerance along with superior
26 corrosion resistance compared to conventional aerospace alloys [1]. Processing Al-Mg-Sc

* Corresponding author. E-mail address: aude.simar@uclouvain.be Postal address: Place Sainte-Barbe 2,
L5.02.02 Louvain-la-Neuve, Belgium, 1348

27 sheets by hot creep forming has gained immense interest in aerospace industry due to the
28 above mentioned properties and absence of spring back effect [3][4]. Recently 5028-H116
29 commercial Al-Mg-Sc alloy sheets have been made available for aerospace applications. Due
30 to its very low density and good mechanical properties, it is a prospective candidate for
31 replacement of many existing Al alloys in industry [5].

32 The main drawback of aluminum-magnesium alloys with Mg \geq 3.5 wt% is the susceptibility
33 to inter-granular corrosion (IGC) when subjected to heating (50°-220 °C) [6]. This susceptibility
34 is due to the precipitation of β (Al₃Mg₂) phase at grain boundaries. The general precipitation
35 sequence in Al-Mg alloys is SSSS (supersaturated solid solution) \rightarrow GP (Guinier Preston) zones
36 \rightarrow β'' (Al₃Mg₂) \rightarrow β' (Al₃Mg₂) \rightarrow β (Al₃Mg₂) [7–9]. In Al-Mg alloys with a Mg content below 18
37 wt%, GP zones and β'' precipitates are only rarely reported. However, the metastable β' and
38 equilibrium β precipitates are the most frequent primary phases observed in low Mg content
39 (<13 wt%) Al alloys, which is the case for 5028 alloy [7–9].

40 The β phase precipitates heterogeneously at grain boundaries (GB), at triple junctions or
41 on pre-existing Mn dispersoids [6, 10]. The GB nucleation sites in Al-Mg alloys are dependent
42 on the GB misorientation [11]. In addition, the dislocation density, type of dispersoids and
43 their density, and the processing temperature also influence precipitation [8, 12, 13]. The
44 diffusion rate of Mg is found to be high in the presence of high dislocation density in Al-Mg
45 alloys [14]. H116 temper rolling is widely accepted as being a corrosion resistant temper in Al-
46 Mg alloys. To the best of our knowledge no detailed studies determine and quantitatively
47 compare the nucleation sites of β phase precipitates formed in heat treated wrought Al-Mg
48 alloys.

49 The electrochemical potential of β (Al_3Mg_2) phase is -1.013V while it is -0.823V for Al [15].
50 Thus, Intergranular corrosion (IGC) occurs due to the anodic corrosion of β (Al_3Mg_2) phase
51 precipitate at the GB [6]. Zhang *et al.* [6] summarized the effect of temperature and time on
52 the degree of sensitization (DOS) of various 5xxx series alloys. Here, sensitization refers to the
53 precipitation of β (Al_3Mg_2) phase when subjected to moderate temperature (50-220°C) for an
54 extended duration [6]. Gaosong *et al.* [10] showed that continuous β phase precipitates favor
55 IGC compared to thicker but discontinuous β precipitate at GB in 5456-H116 aluminum alloy.
56 Wu *et al.* [16] also showed that discontinuous β phase precipitation causes a reduction in
57 corrosion rate in Al-4.6Mg(Mn,Zn) alloy. Zhang *et al.* [17] analyzed the DOS of 5083 alloy
58 comparing various processing methods. They showed that the dominant effect favoring IGC
59 was the grain size (with sub-micrometer grains) compared to GB misorientation.

60 Usual 5xxx series aluminum alloys are strengthened by solid solution hardening and cold
61 working (strain hardening). Thus, the depletion of Mg in the matrix significantly deteriorates
62 the strength when heat treated and sensitized at temperature 50-220 °C, again due to the β
63 phase precipitation [18]. Recent studies have made the 5xxx series alloys heat treatable using
64 Sc as micro-alloying element [19][20]. Limited addition of Sc causes a significant increase of
65 the Al-Mg alloys strength [21]. Sc has also been reported to favor grain refinement in
66 aluminum alloys [20]. Several studies have shown that a thermal treatment of Al-Mg-Sc alloy
67 at 250-350 °C leads to a strength increase due to the formation of Al_3Sc precipitates that pin
68 dislocations [22, 23]. Kendig *et al.* [24] found that the major strengthening effect in Al-Mg-Sc
69 alloy is from the sub-micron grains, followed by Al_3Sc particles and lastly solid solution
70 strengthening of Mg. These Al_3Sc are highly stable with heat treatment and thus the strength
71 of Al-Mg-Sc alloys is retained after heat treatments. This is due to the Zener drag effect which
72 pins dislocations and grain boundaries, also inhibiting recovery and recrystallization [25].

73 The Al-Mg alloy with Sc addition has shown better corrosion resistance post sensitization
 74 at 130 °C for 168 h compared to the alloy without Sc [21]. The mechanical properties after
 75 sensitization are still not known. In general, the sensitization of Al-Mg-Sc alloy on mechanical
 76 and corrosion properties has rarely been reported [21, 26]. Wu *et al.* [16] showed that
 77 annealing Al-Mg alloy at 480 °C for 8 hours increased corrosion resistance during sensitization
 78 at 160 °C for 3 days. This was attributed to the formation of intermittent β phase precipitates
 79 during cooling inside the furnace.

80 The objective of this work is to analyze the effect of the cooling rate on the corrosion
 81 behavior and mechanical properties of a newly developed Al alloy 5028-H116. The Mg wt. %
 82 in this alloy lies in the limit of susceptibility to IGC, however, its corrosion resistance is barely
 83 reported in literature. In addition, the effect of the cooling rate after heat treatment on the
 84 Al-Mg-Sc alloy corrosion resistance but also on the mechanical properties is lacking in
 85 literature. Focus of this work is laid on the effect of some sensitization treatment applied after
 86 hot creep forming and cooling to simulate the in-service behavior of the alloy. The impact on
 87 mechanical and corrosion resistance is explained based on the analysis of the changes in the
 88 β (Al_3Mg_2) phase precipitation sites under different cooling conditions.

89 2. Materials and methods

90 The aluminum alloy considered in this study is the Al-Mg-Sc 5028 alloy with a sheet thickness
 91 of 4.7 mm. The as received (AR) 5028-H116 alloy has undergone cold rolling until H116
 92 temper. The composition of the alloy is provided in Table 1.

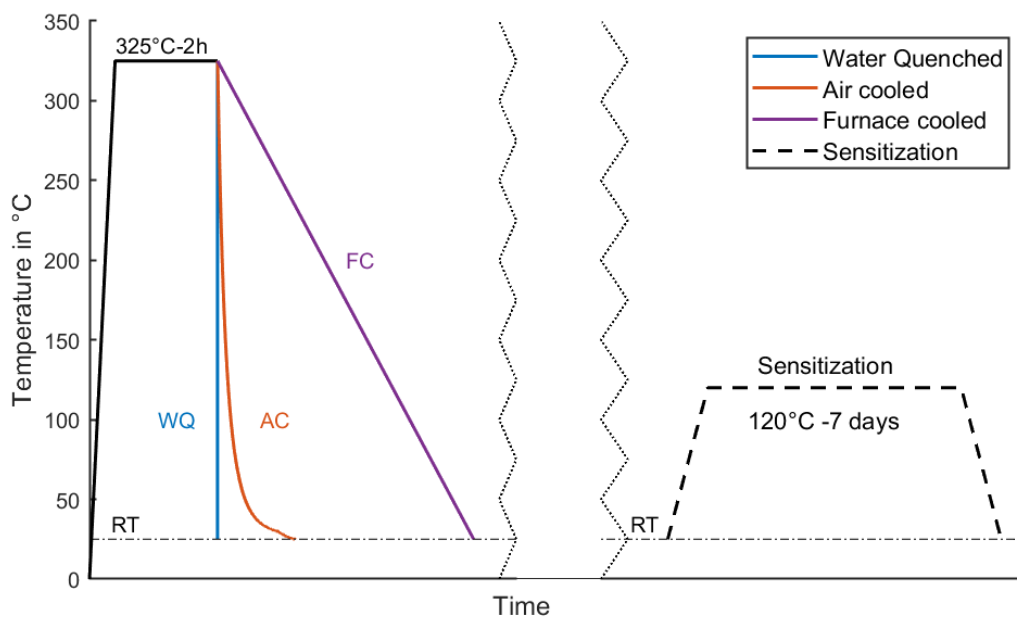
93 *Table 1: AR 5028-H116 alloy chemical composition in wt%. (rest Al content)*

Element	Si	Fe	Cu	Mn	Mg	Cr	Zn	Ti	Zr	Sc
Wt.%	0.0-0.3	0.0-0.4	0.0-0.2	0.3-1.0	3.2-4.8	0.05-0.15	0.05-0.50	0.05-0.15	0.05-0.15	0.02-0.40

94

95 The alloy AR 5028-H116 was annealed at 325 °C for 2 hours. The annealing temperature
96 and time are representative of creep forming thermal conditions [3]. Three different cooling
97 rates were compared (see Figure 1): Water Quenching (WQ) with water at room temperature,
98 Air Cooling (AC) and controlled Furnace Cooling (FC). The WQ, AC and FC materials were
99 additionally subjected to heat treatment at 120 °C for 7 days, which here is called
100 “sensitization heat treatment”. Sensitized conditions are called: WQ+S, AC+S and FC+S.

101 The microstructure characterization was conducted using an Olympus optical microscope
102 and ZEISS ULTRA-55 scanning electron microscope (SEM) equipped with energy dispersive X-
103 Ray (EDX) system. Electron backscatter diffraction (EBSD) mapping was performed with a field
104 emission gun SEM (SigmaTM, Zeiss) equipped with a Symmetry S2 EBSD detector.



105
106 *Figure 1: Schematic of the heat treatment and cooling rate applied on AR 5028-H116*
107 *aluminum alloy (RT = Room Temperature).*

108 Transmission electron microscopy (TEM) specimens were prepared by mechanical
109 polishing followed by ion milling using Gatan Duo 691 precision ion polishing system (PIPS).

110 STEM-EDX mapping and STEM high-angle annular dark-field detector (STEM-HAADF) images
111 were acquired using a FEI Tecnai Osiris TEM operated at 200 kV and equipped with a highly
112 efficient SuperX system. The post-treatment of the EDX data was carried using Bruker ESPRIT
113 software. The statistical analysis of the β phase precipitates were computed using ImageJ
114 software. Around 40-50 precipitates were considered under each condition for the
115 quantitative analysis. The nearest neighbor distance (NND) was computed based on the
116 distance between each β precipitate and its closest neighbor.

117 Differential scanning calorimetry (DSC) was performed with a Netzsch DSC 404 C Pegasus
118 model equipment. The DSC samples were extracted from heat treated materials by micro-
119 cutting. The weight of all the DSC samples was chosen to be ~ 40 mg, to obtain a good signal
120 to noise ratio. The specimens were heated at a constant rate of 10 °C/min in argon
121 atmosphere. The identification and analysis of the DSC curves and peaks were based on
122 literature [7, 27]. The baseline signal was subtracted from the DSC signal curves to identify the
123 phase transition peaks. The area below these phase transition peaks indicates the enthalpy of
124 formation/dissolution of the phase. Milkereit *et al.* [28] have shown that the precipitation
125 enthalpy measured by DSC is directly proportional to the atomic or volume fraction of
126 precipitates.

127 The Vickers micro-hardness testing was conducted under a load of 200 g with a dwell time
128 of 15s following ISO 6507-2:2018 [29] on an Emco-Test Durascan 5G equipment. The tensile
129 test specimens were machined following ASTM E8 standard [30] (sub size specimen) with the
130 tensile direction taken along the rolling direction. The tensile tests were performed on a Zwick
131 50 kN tensile machine with an extensometer throughout the test and loaded at a constant
132 rate of 1 mm/min. The data acquisition frequency was set to 100 Hz. The extensometer gauge

133 length was 20 mm. Four tests per condition were performed to assess reproducibility. The
134 true fracture strain is here defined as $\varepsilon_f = \ln\left(\frac{A_o}{A_f}\right)$, where A_o is the initial area and A_f is the
135 final area at fracture.

136 Nitric acid mass loss test (NAMLT) was carried out to determine the susceptibility to IGC
137 following ASTM-G67 standard [31]. The corrosion test (CT) samples of dimension 50 mm x 6
138 mm x 4.7 mm were extracted by micro-cutting with the 50 mm dimension along the rolling
139 direction followed by standard polishing with SiC paper (#600 grit). The cross sections of
140 corrosion test samples were examined by optical microscopy. The polished specimens were
141 etched using Keller etchant to observe the grain structure after corrosion.

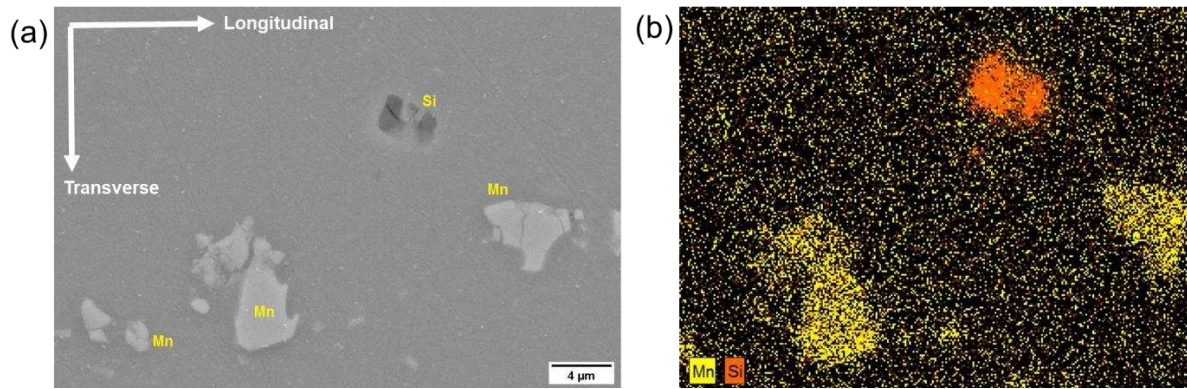
142

143 **3. Results**

144 *3.1. Microstructure observation*

145 *3.1.1. Coarse intermetallic phases*

146 A SEM micrograph of the as received (AR) alloy 5028-H116 is shown in Figure 2. The EDX maps
147 shows the presence of Mn and Si rich intermetallics in the aluminum matrix. Similar SEM
148 observations were carried out for heat treated and sensitized conditions and no significant
149 difference in these intermetallics distribution and size was found. These intermetallics were
150 aligned mostly along the longitudinal rolling direction.

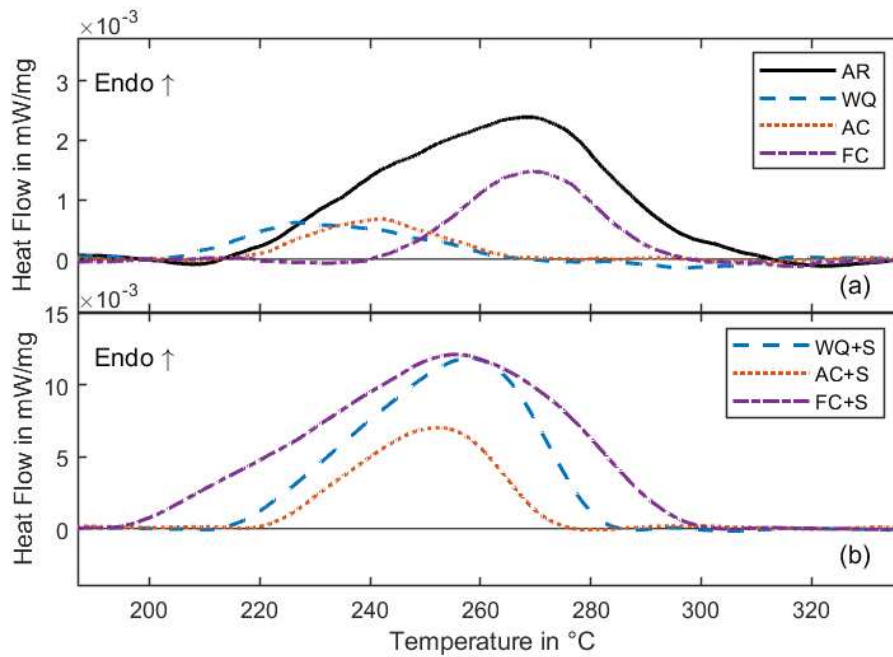


151

152 *Figure 2: (a) SEM micrograph of the as received (AR) 5028-H116 aluminum alloy providing an*
153 *overview of the microstructure and (b) an EDX map of the microstructure identifying Mn and*
154 *Si rich intermetallics.*

155 3.1.2. β precipitation

156 The amount of β (Al_3Mg_2) precipitates formed in 5028- H116AA can be identified by DSC for
157 various heat treatments. Figure 3 shows the DSC responses of non-sensitized and sensitized
158 alloy (see supplementary Figure S1 for the full curve). The analysis is carried out only on the
159 heating DSC curves, as our focus is on the identification of pre-existing phases. The
160 endothermic peak observed around 280-300 °C is attributed to β phase dissolution, following
161 Ref. [7, 27].

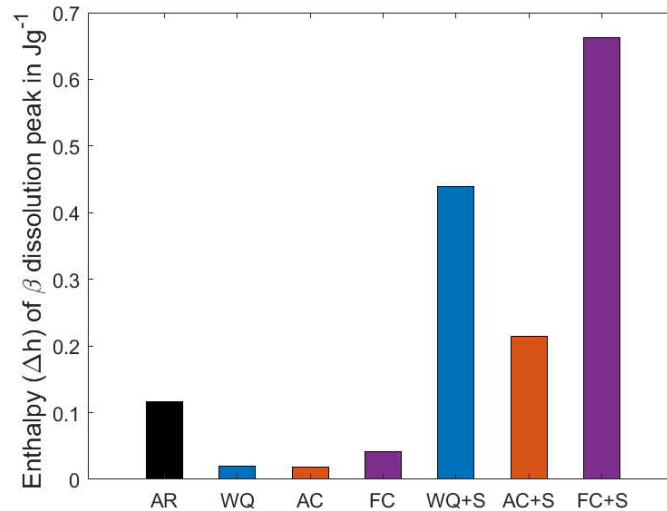


162

163 *Figure 3: DSC heating curves showing the β phase endothermic dissolution peaks for (a) non-*
 164 *sensitized conditions and (b) sensitized conditions. Note the difference in scale between Figures*
 165 *(a) and (b) required by the much larger peak observed for the sensitized samples.*

166 Figure 3 shows that the β dissolution peak is varying with respect to the heat treatment
 167 conditions. In general, the area under the dissolution peak indicates the volume fraction of
 168 pre-existing phases [28]. Thus, the area under the β dissolution peak (Figure 4) is proportional
 169 to the volume fraction of β precipitates in the heat-treated conditions. Observing the non-
 170 sensitized conditions, the volume fraction of β precipitates is larger in the AR alloy compared
 171 to WQ, AC and FC conditions. Among WQ, AC and FC conditions, an increase in cooling rate
 172 decreases the volume fraction of β precipitates. Now, the overall volume fraction of β
 173 precipitates after the 325 $^{\circ}\text{C}$ heat treatment is much lower than after the sensitization
 174 treatment. The cooling rate dependency of the volume fraction of β precipitates post
 175 sensitization is more significant. The FC+S condition presents the highest volume fraction of β
 176 precipitates followed by the WQ+S and finally AC+S condition. Here, the effect of the heat

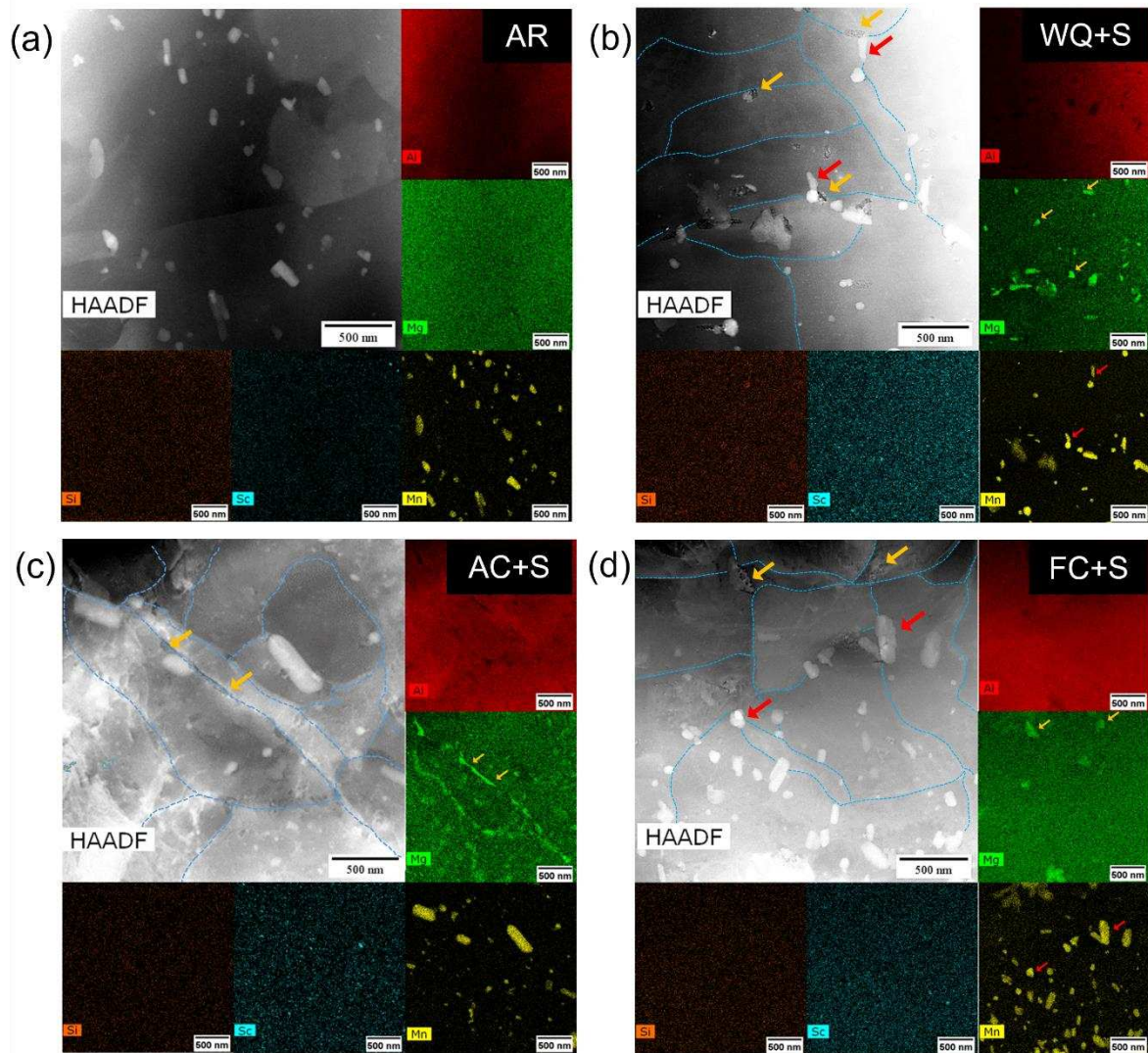
177 treatment cooling rate is thus not monotonous.



178

179 *Figure 4: Enthalpy of the β dissolution peak which is proportional to the volume fraction of β*
180 *precipitates for the various heat treatment conditions.*

181 To clarify this difference in β (Al_3Mg_2) precipitation among the sensitized conditions (Figure
182 4), HAADF-STEM imaging was carried out to determine the actual distribution of Mg rich β
183 phase precipitates. The STEM micrographs are shown in Figure 5 for AR and sensitized (WQ+S,
184 AC+S, FC+S) conditions. EDX elemental maps showing the distribution of Al, Mg, Mn, Sc and Si
185 are also provided. In Figure 5, the EDX map confirms the presence of β precipitates that appear
186 as sparingly distributed Mg-rich clusters. In addition, small Mn-rich intermetallics can be
187 observed in the matrix. The distribution of Sc is not evident in Figure 5. Figure 6(a-b) show
188 dispersed Sc-rich precipitates that appear in the form of kidney structure or as pair of coffee
189 beans. These typical structures were reported previously by Yin *et al.* [32] and are expected
190 to be Al_3Sc precipitates [33]. Further STEM-EDX mapping was performed at higher
191 magnification to reveal the Sc enrichment as shown in Figure 6(c-d).

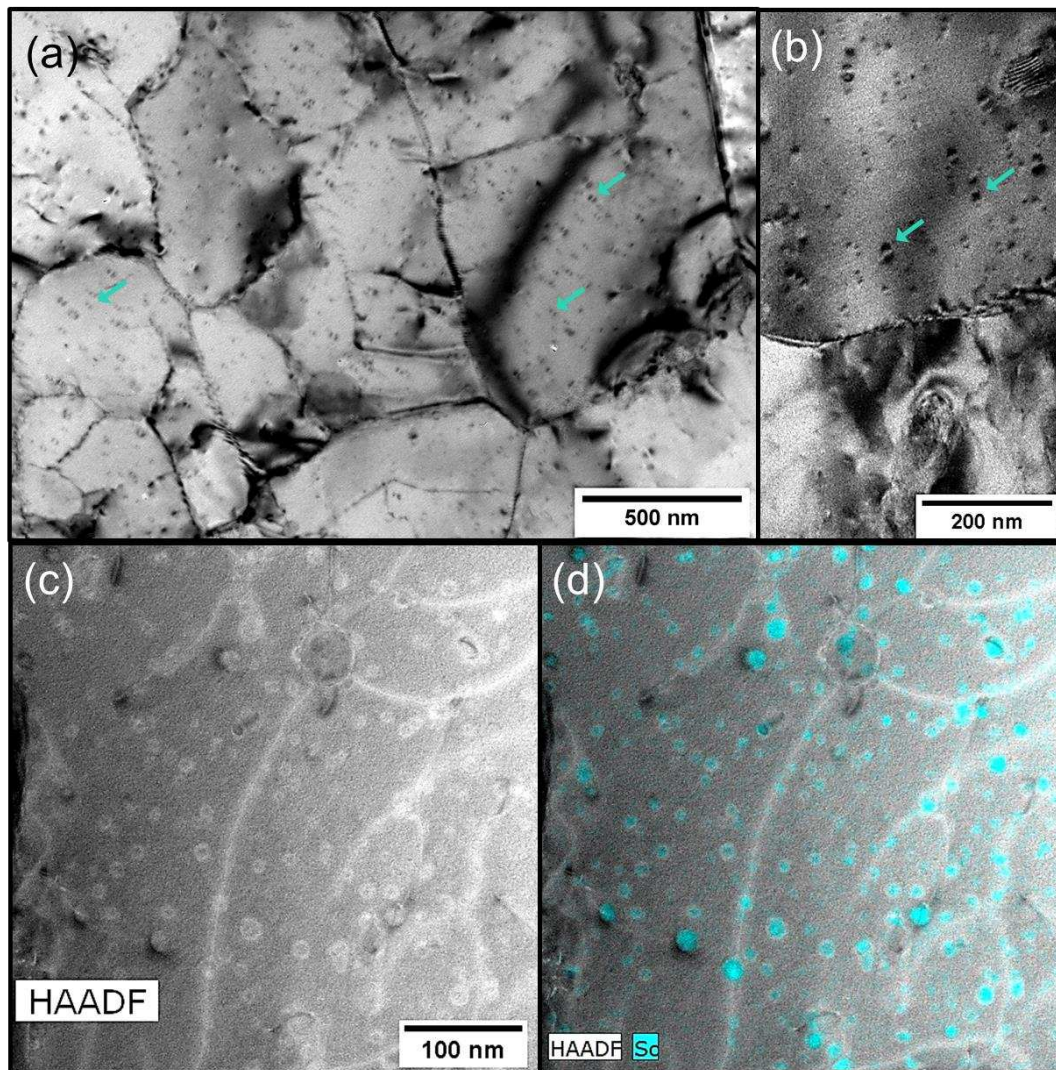


192

193 *Figure 5: STEM images with associated EDX elemental maps showing the alloying element*
 194 *distribution in (a) AR (b) WQ+S (c) AC+S (d) FC+S of 5028-H116 aluminum alloy (blue lines*
 195 *highlight grain boundaries, yellow arrows highlight β precipitate, and red arrows highlight Mn-*
 196 *rich dispersoids).*

197 In WQ+S condition (Figure 5b), thick β phase precipitates can be observed along grain
 198 boundaries and inside grains (yellow arrow in Figure 5b). These precipitates are located
 199 adjacent to Mn-rich intermetallics and are rarely independent of Mn intermetallics (red arrow
 200 in Figure 5b). In AC+S (Figure 5c) condition, thin elongated β phase precipitates are formed at

201 grain boundaries as observed in the Mg map. In FC+S condition (Figure 5d), the β precipitates
202 are much larger and are found mostly at GB triple junctions.

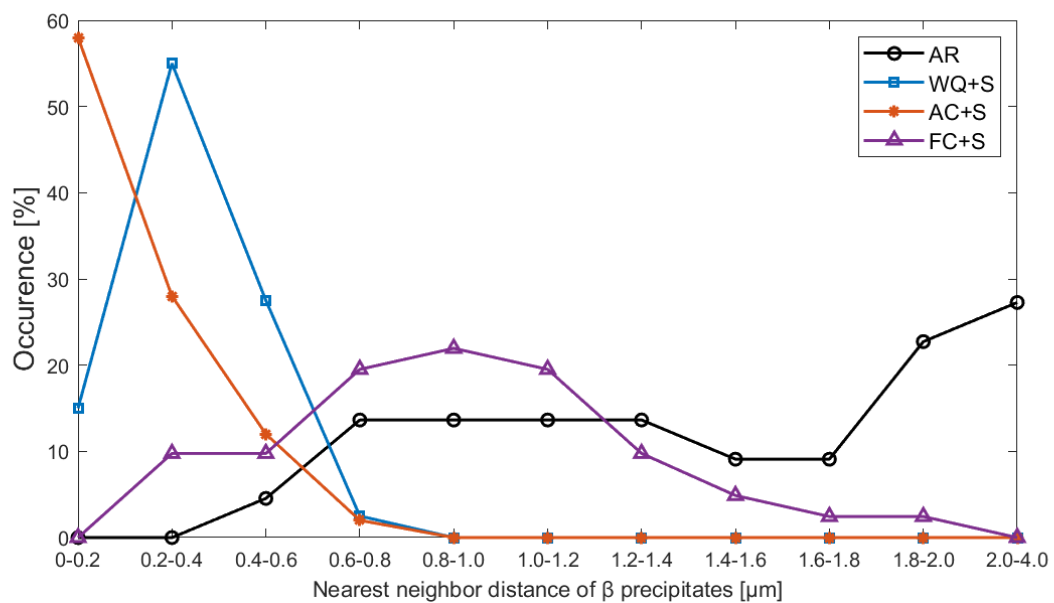


203

204 *Figure 6: (a) TEM images showing the presence of Al_3Sc precipitates in WQ+S condition (b)*
205 *higher magnification TEM image showing Al_3Sc precipitates, (c) HAADF-STEM image in WQ+S*
206 *condition and (d) shows STEM image in (c) overlaid with Sc enriched precipitates.*

207 Figure 7 quantifies the nearest neighbor distance (NND) of β precipitates as a function of
208 occurrence in different heat treatment condition computed from the TEM images. In the AR
209 condition, the β precipitates are observed at a neighboring distance larger than $0.6 \mu m$ and
210 even mostly higher than $2 \mu m$ from each other. Among sensitized alloys, in the AC+S, β

211 precipitates are found typically at a NND lower than 0.2 μm , while in the WQ+S condition the
 212 NND ranges generally between 0.2 - 0.4 μm which are both close to a continuous arrangement
 213 of β precipitates. Whereas in FC+S sample the precipitates are distributed far away from each
 214 other mostly between 0.6 - 1.2 μm , hence the largest spacing between β precipitates among
 215 all sensitized conditions (WQ+S, AC+S, FC+S).

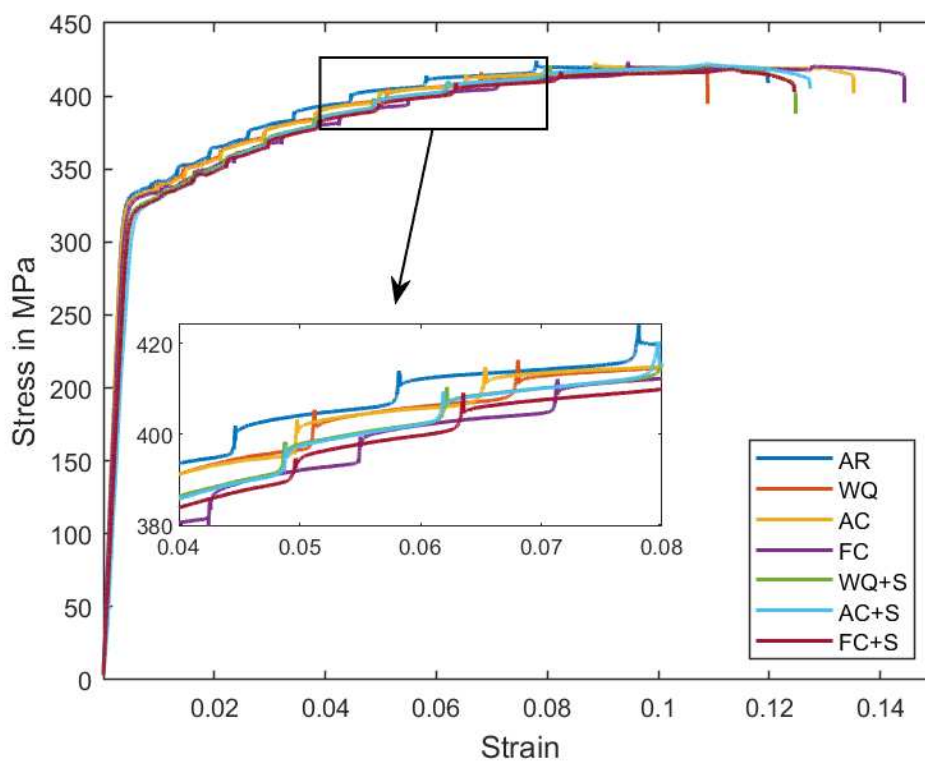


216
 217 *Figure 7: 2D Distribution of nearest neighbor distance (NND) in different heat treated condition*
 218 *extracted from TEM images. The “occurrence” is calculated as the ratio of population in the*
 219 *group divided by the total number of measurements for each heat treated condition.*

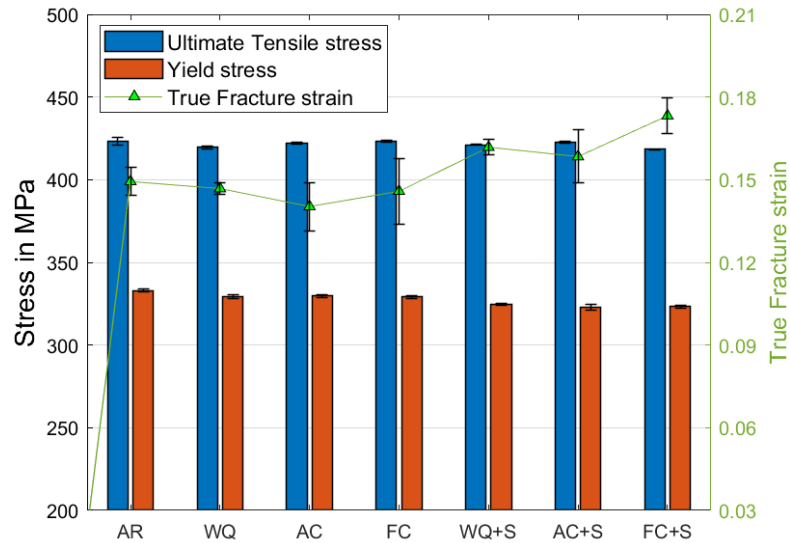
220 3.2. Mechanical properties

221 Tensile and micro-hardness (see supplementary Figure S2) tests were conducted to study the
 222 effect of thermal treatment and cooling rate on the mechanical behavior of the 5028-H116 Al
 223 alloy. Uniaxial tensile test responses are shown in Figure 8 for the as received (AR), heat
 224 treated and sensitized conditions. The tensile stress-strain curves (Figure 8) exhibit stress
 225 serrations which are generally observed in Al-Mg alloys and correspond to the Portevin–Le

226 Chatelier (PLC) effect (see supplementary Figure S3 for individual plots). Figure 9 reports the
227 corresponding ultimate tensile strength, yield stress and fracture strain. The variation in the
228 tensile strength among AR, heat treated (WQ, AC, FC) and sensitized (WQ+S, AC+S, FC+S)
229 conditions is <1 %. Whereas the yield stress is reduced by about 1.2 % among heat treated
230 (WQ, AC, FC) conditions compared to AR material and about 3.0 % for sensitized (WQ+S, AC+S,
231 FC+S) specimens. The micro-hardness is identical in all conditions (~117 HV) within the error
232 of the measurement (see supplementary Figure S2).



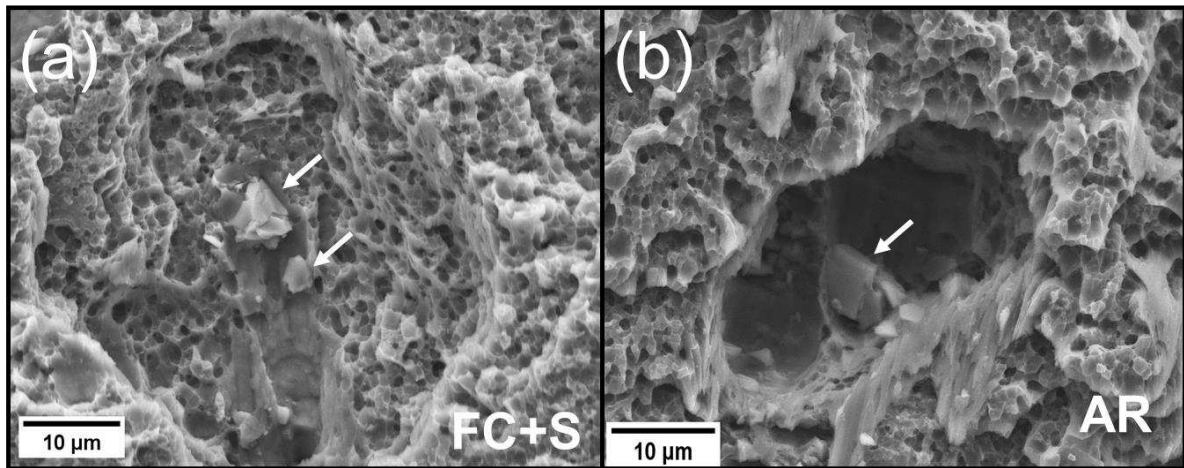
233
234 *Figure 8: Uniaxial tensile test stress-strain curves of AR and different heat treated 5028-H116*
235 *Al alloy highlighting the PLC serrations in the sub-figure.*



236

237 *Figure 9: Ultimate tensile strength, yield stress and true fracture strain of AR, heat treated*
 238 *materials following different cooling rates and sensitized thermal treatments. Error bars are*
 239 *systematically provided.*

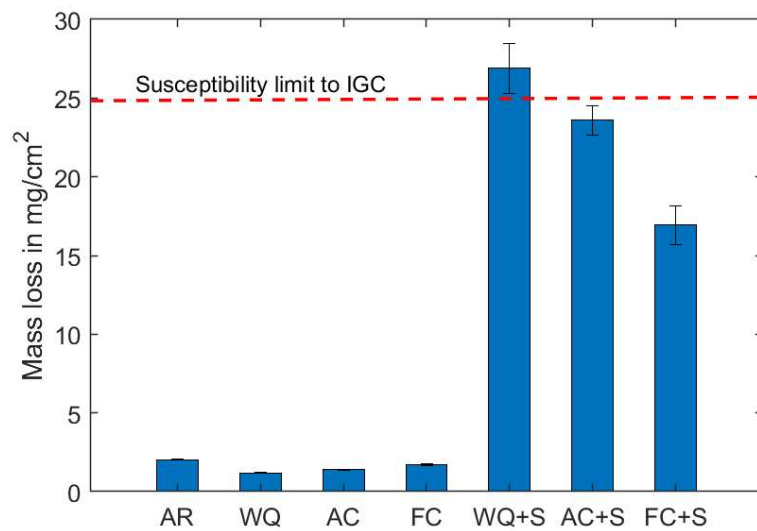
240 Figure 10 shows fracture surfaces of tensile specimens of the two extreme conditions
 241 (FC+S and AR) featuring two populations of void sizes. Ductile shear fracture is caused by the
 242 nucleation and growth of larger voids caused by fracture or decohesion of the large
 243 intermetallics. This can be identified by the intermetallic indicated by the white arrows in
 244 Figure 10. Now, final void coalescence seems to be triggered by a secondary population of
 245 sub-micron sized cavities visible throughout the fracture surface. These cavities are expectedly
 246 initiating on β precipitates based on the cavity size. The fracture surface among AR, heat
 247 treated (WQ, AC, FC) and sensitized (WQ+S, AC+S, FC+S) conditions do not evidence any clear
 248 difference in damage mechanism.



249

250 *Figure 10: Fracture surface of (a) FC+S and (b) AR condition. The white arrows points to the Mn*
 251 *rich intermetallic that expectedly lead to the nucleation of a large void.*

252 *3.3. Corrosion resistance*

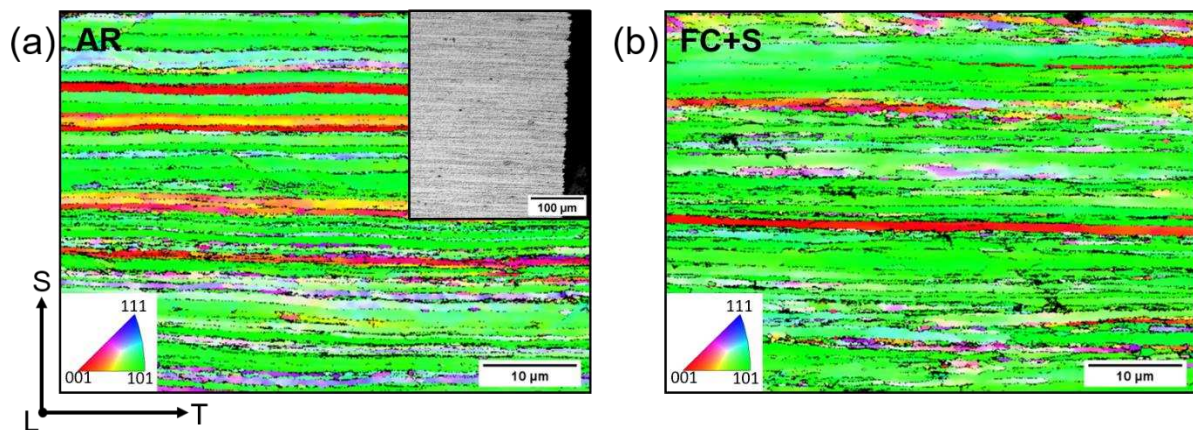


253

254 *Figure 11: Nitric acid mass loss test [NAMLT] results for different heat treatment conditions of*
 255 *5028-H116 Al alloy.*

256 The NAMLT corrosion test mass loss results are provided in Figure 11. It shows that the AR
 257 5028-H116 and annealed conditions (WQ, AC, FC) with different cooling rates involve mass
 258 losses below 3 mg/cm², indicating a high resistance to intergranular corrosion (IGC)

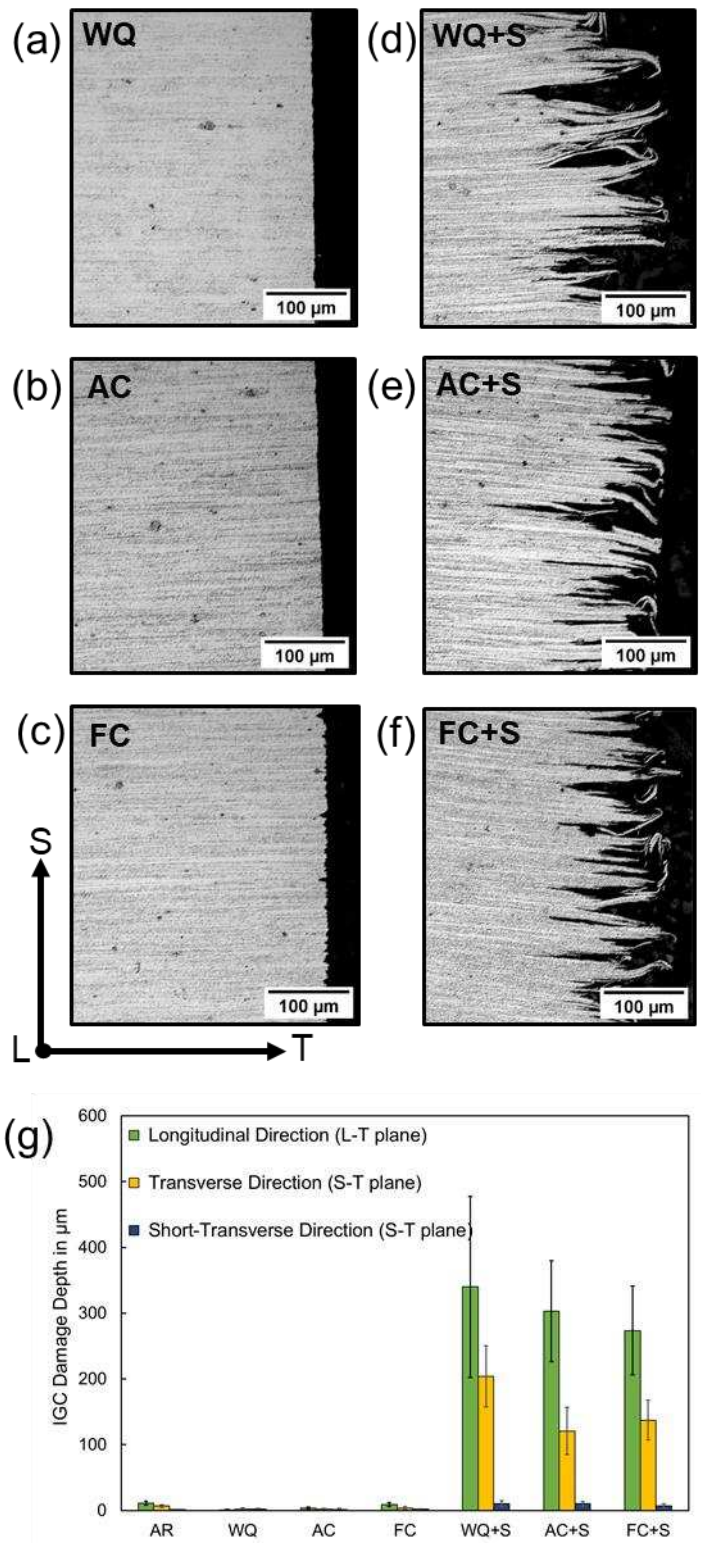
259 <25mg/cm²) [31]. In general, annealing at 325 °C (WQ, AC, FC) leads to a slight mass loss
 260 reduction compared to that of AR 5028-H116. Conversely, the sensitization of these annealed
 261 materials (WQ+S, AC+S, FC+S) shows a significant increase in mass loss. In addition, Figure 11
 262 shows significant impact of the cooling rate on sensitized conditions. Among the sensitized
 263 conditions the mass loss of WQ+S specimen is over the standard limit of susceptibility to IGC
 264 [31], while AC+S condition is rather close to the susceptibility limit and FC+S condition presents
 265 a higher resistance to IGC.



266
 267 *Figure 12: EBSD IPF map providing the grains texture along S-T plane (a) AR condition, Inset:*
 268 *AR corroded sample indicating corrosion damage and etched to visualize grain orientation. (b)*
 269 *FC+S condition.*

270 The corrosion mechanism can be better understood by looking at the grain morphology.
 271 EBSD maps of Figure 12a and 12b represent the elongated grains in the short transverse (S-T)
 272 plane of the two extreme conditions: AR and FC+S. No grain growth could be evidenced
 273 following the heat treatment at 325 °C and sensitization (compare FC+S condition to AR
 274 condition in Figure 12). Figure 12a (inset) and 13 show the cross-sectional view of the
 275 corrosion test samples along the S-T plane. The AR (Figure 12a-inset) and annealed conditions
 276 (WQ, AC, FC) (Figure 13 a,b,c) did not exhibit any noticeable corrosion damage. On the

277 contrary, significant corrosion penetration cracks are observed in the sensitized conditions
278 (WQ+S, AC+S, FC+S), see Figure 13 d,e,f. Comparing these results with the grain structure
279 (Figure 12 a,b), the corrosion damage pattern confirms that IGC is the dominant corrosion
280 mechanism occurring in the heat treated 5028-H116 Al alloy. The IGC appearance in rolled
281 alloys significantly depends on the grain morphology with an elongation in the rolling direction
282 [34]. Thus, the corrosion penetration depth was quantified along the Longitudinal (L),
283 Transverse (T) and Short-transverse (S) directions and is presented in Figure 13g. The corrosion
284 penetration indicates the corrosion rate, which is found to be severe along L direction, slightly
285 less severe along the T direction and minimum along the S direction. This is particularly visible
286 in the sensitized conditions.



287

288 *Figure 13: Heat treated 5028-H116 corroded samples indicating corrosion damage in the S-T*

289 *plane and etched to visualize grain orientation for various heat treatment conditions: (a) water*

290 *quenched [WQ], (b) air cooled [AC], (c) furnace cooled [FC], (d) water quenched and sensitized*

291 *[WQ+S], (e) air cooled and sensitized [AC+S], (f) furnace cooled and sensitized [FC+S]. (g) IGC*

292 Corrosion damage depth quantified in Longitudinal, Transverse and Short-Transverse direction
293 for the various heat-treated conditions of 5028-H116 alloy.

294 4. Discussion

295 The tensile test results (Figure 9) do not indicate any significant variation of tensile strength
296 due to heat treatment at 325 °C and cooling rate nor due to sensitization. This could be directly
297 linked to the role of Al₃Sc precipitates present in the heat treated 5028 Al alloy (Figure 6). In
298 addition, non-recrystallized submicron grains observed in Figure 12 explain stable mechanical
299 properties. In general, the formation of β -phase (Al₃Mg₂) precipitates in Al-Mg alloys is known
300 to reduce the strength of the alloy when heat treated [18]. This effect is not observed in our
301 study, due to the formation of dominating Al₃Sc strengthening precipitates, see also Kendig *et*
302 *al.* [24]. Jambu *et al.* [4] concluded that the thermally stable Al₃Sc precipitates [35] are the
303 reason for the thermal stability of the 5024 aluminum alloy strength. Xu *et al.* [36] also showed
304 that Al₃Sc precipitates are highly stable and coherent in Al-Mg-Sc alloys when annealed at 300-
305 450 °C for up to 168 h.

306 In addition, the tensile curves (Figure 8) exhibit characteristic increases and drops in flow
307 stress. This behavior has already been observed in the Al-Mg-Sc alloy by Mogucheveva *et al.* [37]
308 and was associated to the dispersed Al₃Sc precipitates which pin the gliding dislocations. Their
309 unpinning at higher stress leads to these sudden stress jumps. The observed serrations are
310 identical in all conditions (Figure 8) and have been attributed to A-type serrations, see Zhang
311 *et al.* [38] for additional details. A change in the pattern of serrations is generally observed
312 when there is a change in the testing temperature, applied strain or a difference in grain
313 morphology [38]. As our EBSD measurements (Figure 12) do not highlight any difference in
314 grain morphology and size after the 325 °C heat treatment and, as similar testing conditions

315 (temperature and strain rate) were applied, identical serration patterns are expected to be
316 observed. The β phase precipitates do not either seem to influence the stress flow in this new
317 5028 aluminium alloy.

318 The sensitization heat treated conditions lead to some increased fracture strain (Figure 9)
319 when compared to the equivalent non-sensitized condition. Sensitization treatment promotes
320 the formation of a higher volume fraction of β (Al_3Mg_2) precipitates as concluded from the
321 DSC results (Figure 4). Thus, the small increase in fracture strain is possibly due to the
322 interaction of dislocations with β (Al_3Mg_2) precipitates as well as with the Al_3Sc precipitates.
323 In this context, it is worth noticing that the Sc-enriched precipitates are preferentially seen on
324 or around dislocations (Fig. 6 (c-d)). The pinning of dislocations and sub-grain boundaries on
325 the Sc rich precipitates has been reported by Liu *et al.* [39]. Overall, no significant effect of the
326 heat treatment is observed on the mechanical properties.

327 Concerning the corrosion behavior, the mass loss (Figure 11) shows the same trend as the
328 IGC penetration depth (Figure 13). Lim *et al.* [34] showed that corrosion in Al-Mg alloys occurs
329 along the GB and once the complete GB is corroded, the grain falls out in the wake leading to
330 a pit at the surface. The reduction of mass loss in the annealed condition (WQ, AC, or FC)
331 compared to that of AR 5028-H116 can be attributed to the dissolution of pre-existing β phase
332 precipitates when annealed at 325 °C. Consequently, the volume fraction of β phase
333 precipitates in annealed conditions (WQ, AC, FC) is lower than in the AR 5028 Al alloy (Figure
334 4) delaying corrosion. The significant increase in volume fraction of β precipitates after the
335 sensitization heat treatment (Figure 4) is related to the lower corrosion resistance reported in
336 Figure 11.

337 Table 2 summarizes the results of the observations made in section 3 and will help the
 338 reader to follow the discussion that comes afterwards.

339

340 *Table 2: Summary of experimental results for different heat treatment conditions on the*
 341 *5028-H116 Al alloy.*

Specimen	Corrosion mass loss [mg/cm ²]	DSC area proportional to volume fraction of β precipitates [J/g]	Nearest neighbor distance of β precipitates [nm]	Thickness of β precipitates [nm]
WQ+S	26.8 ± 1.5	0.44	340 ± 118	50 ± 21
AC+S	23.6 ± 0.9	0.21	230 ± 136	41 ± 19
FC+S	16.9 ± 1.2	0.67	902 ± 364	111 ± 44

342

343 The significant effect of cooling rate on the corrosion resistance of sensitized samples
 344 (WQ+S, AC+S, FC+S) is evident in Figure 11. The general trend shows that an increase in cooling
 345 rate after annealing at 325 °C increases the IGC (Table 2). For the WQ+S and AC+S conditions,
 346 IGC susceptibility (Figure 13) can be directly related to their volume fraction of β precipitates.
 347 Now, the FC+S condition presents the lowest susceptibility to IGC among all sensitized
 348 conditions (Figure 11 and 13). Unexpectedly, that condition also holds the highest volume
 349 fraction of β precipitates among all sensitized conditions (WQ+S, AC+S, FC+S) (Table 2). This
 350 apparent inconsistency leads to the proposition that a higher volume fraction of β phase
 351 precipitates does not systematically exhibit higher susceptibility to IGC. The precipitate
 352 distribution plays a major role on its susceptibility to corrosion.

353 The nucleation sites of β phase precipitation are known to be heterogeneous. The cooling
 354 rate shows clear effects on β precipitates distribution in sensitized condition by their

355 nucleation on Mn dispersoids, grain boundaries or triple junctions with decreasing cooling
356 rate, as evidenced by the TEM results of Figure 5. Ding *et al.* [40] explained the transition of β
357 precipitates nucleation sites at 220 °C from GB to triple junction using classical nucleation
358 theory in 5083 Al alloy containing erbium and zirconium. According to their study, the
359 nucleation rate at GB triple junctions is 10 times higher than at the GB at 220 °C. At a lower
360 temperature (100-150 °C), the nucleation rate is 100 times higher at GB than at GB triple
361 junctions. This can be related to the TEM observations in Figure 5 for the FC+S condition,
362 where the β precipitates nucleate at GB triple junctions during the furnace cooling (FC) and
363 grow during sensitization. Similarly, for the AC+S sample the air-cooling curve (Figure 1)
364 exhibits a slight reduction in cooling rate at around 170 °C and below, leading to a higher
365 nucleation rate of β precipitates at grain boundaries in AC+S condition (Figure 5c). Zhu *et al.*
366 [41] found Mn rich intermetallics are low energy barrier sites for β precipitate nucleation at
367 low temperature. It is the case for WQ+S condition when subjected to sensitization, see Figure
368 5b. Hence, as a summary, the rate of β precipitate nucleation at different nucleation sites is a
369 function of temperature. The change in temperature due to different cooling rates led to a
370 shift of nucleation sites towards lower energy sites.

371 During sensitization, Mg atoms diffuse towards pre-existing β precipitates as the
372 nucleation at lower temperature requires higher energy. Thus, the growth of β precipitates is
373 favored at the detriment of their nucleation in AC+S and FC+S samples [14, 42]. The
374 phenomenon of quenched-in vacancies explains the role of trapped vacancies due to rapid
375 cooling from high temperature [43]. These vacancies then migrate to lower nucleation energy
376 sites, e.g. the edges of the Mn dispersoids. This then drives the precipitate nucleation and
377 growth during sensitization in the WQ+S sample.

378 The perfect continuity of β phase precipitates is known to be crucial for IGC in sensitized
379 Al-Mg alloys [6, 10]. Continuous β phase precipitates increase IGC rate due to uninterrupted
380 difference in corrosion potential. Among sensitized conditions, the AC+S condition exhibits
381 continuous thin β phase precipitates along the GB (see Table 2 and Figure 5c). The WQ+S
382 condition exhibits rather continuous thick β phase precipitates along GBs adjacent to Mn
383 dispersoids (see Table 2 and Figure 5b). The WQ+S condition displays a higher mass loss as the
384 IGC penetration depth is larger in the WQ+S sample compared to the AC+S sample. This
385 suggests that the rather continuous thick β precipitates of higher volume fraction (sample
386 WQ+S, see Table 2) are more vulnerable to corrosion than continuous thin β precipitates with
387 a lower volume fraction of β precipitates (sample AC+S, see Table 2). Whereas, in the FC+S
388 condition the β precipitates are formed at GB triple junction (Figure 5d) which are far apart
389 from each other compared to AC+S and WQ+S conditions (Figure 7), this significantly reduces
390 the local corrosion potential along GB favoring a better resistance to corrosion of the FC+S
391 condition compared to all other sensitized conditions. To summarize, the main difference in β
392 precipitate distribution causing the better corrosion resistance of the FC+S sample is actually
393 associated to the precipitate inter-distance.

394 5. Conclusion

395 The influence of cooling rate during heat treatments on the mechanical and corrosion
396 properties of aluminum alloy 5028-H116 was investigated. The annealing at 325 °C followed
397 by sensitization heat treatment at 120 °C for 7 days did not significantly affect the strength of
398 the alloy. The low fracture strain of the alloy is slightly increased by the annealing and
399 sensitization heat treatment which is proposed to be due to a larger β (Al_3Mg_2) precipitates
400 volume fraction. But, overall, this effect is rather limited. On the contrary, the sensitization

401 heat treatment significantly increases the corrosion mass loss of 5028-H116 aluminium alloy.

402 The main findings of this study are:

403 1. The cooling rate after this 325 °C heat treatment has a significant impact on the site of
404 nucleation and growth of β (Al_3Mg_2) precipitate during the following sensitization heat
405 treatment.

406 2. The β (Al_3Mg_2) precipitate distribution critically affects intergranular corrosion (IGC) in
407 addition to the better known effect of β (Al_3Mg_2) volume fraction.

408 3. The IGC rate can be decelerated by nucleating the β (Al_3Mg_2) phase precipitates at
409 triple junction GB using slow (furnace) cooling after the 325 °C annealing treatment.

410 Thus, this study has demonstrated that implementing slow (furnace) cooling after annealing
411 5028-H116 at 325 °C is advantageous in increasing the resistance to IGC after a sensitization
412 heat treatment.

413 **Declaration of competing interest**

414 The authors declare that they have no known competing financial interests or personal
415 relationships that could have appeared to influence the work reported in this paper.

416 **Acknowledgements**

417 Novelis is acknowledged for providing the material and for technical support.

418 **Data availability**

419 The raw/processed data required to reproduce these findings cannot be shared online at this
420 time but can be asked to the corresponding author upon reasonable request.

421 **References**

422

- 423 1. Ereemeev, N. V, Predko, P. Y., Ereemeev, V. V, Bespalov, A. V, & Bochvar, S. G. (2021).
424 Technological Aspects of Thin Plate Production for Aircraft Construction Based on Al–
425 Mg–Sc Alloys. *Inorganic Materials: Applied Research*, 12(2), 288–295.
426 <https://doi.org/10.1134/S2075113321020131>
- 427 2. Mann, V. K., Krokhin, A. Y., Alabin, A. N., Frolov, V. F., Redkin, I. A., & Vahromov, R. O.
428 (2016). Al-Mg-Sc alloys for sheet, plate, and additive manufacturing for automotive
429 and aerospace. *Light Metal Age*, 74(5), 12–16. Retrieved from
430 <https://elibrary.ru/item.asp?id=29551799>
- 431 3. Zimmermann, F., Brosius, A., Beyer, R. E., Standfuß, J., Jahn, A., & Banke, D. (2018).
432 Creep forming of very thin AlMgSc sheets for aeronautical applications. In *Procedia*
433 *Manufacturing* (Vol. 15, pp. 1008–1015). Elsevier.
434 <https://doi.org/10.1016/j.promfg.2018.07.393>
- 435 4. Jambu .S, Lenczowski .B, Rauh R, J. K. (2002). Creep forming of AlMgSc alloys for
436 aeronautic and space applications. In *Proceedings of the 23rd International Congress*
437 *of Aeronautical Sciences*.
- 438 5. Vorel, M., Hinsch, S., Konopka, M., & Scheerer, M. (2017). AlMgSc alloy 5028 status of
439 maturation. *7Th European Conference for Aeronautics and Space Sciences (Eucass)*.
440 <https://doi.org/10.13009/EUCASS2017-633>
- 441 6. Zhang, R., Knight, S. P., Holtz, R. L., Goswami, R., Davies, C. H. J., & Birbilis, N. (2016). A
442 survey of sensitization in 5xxx series aluminum alloys. In *Corrosion* (Vol. 72, pp. 144–
443 159). <https://doi.org/10.5006/1787>
- 444 7. Starink, M. J., & Zahra, A. M. (1998). β' and β precipitation in AN Al-Mg alloy studied
445 by DSC and TEM. *Acta Materialia*, 46(10), 3381–3397. [https://doi.org/10.1016/S1359-](https://doi.org/10.1016/S1359-6454(98)00053-6)
446 [6454\(98\)00053-6](https://doi.org/10.1016/S1359-6454(98)00053-6)
- 447 8. Scotto D’Antuono, D. (2017). *β Phase Growth and Precipitation in the 5xxx Series*
448 *Aluminum Alloy System. Ph. D. Thesis*. Drexel University.
- 449 9. Goswami, R., Spanos, G., Pao, P. S., & Holtz, R. L. (2010). Precipitation behavior of the
450 β phase in Al-5083. *Materials Science and Engineering: A*, 527(4–5), 1089–1095.
451 <https://doi.org/10.1016/j.msea.2009.10.007>
- 452 10. Yi, G., Cullen, D. A., Littrell, K. C., Golumbskie, W., Sundberg, E., & Free, M. L. (2017).
453 Characterization of Al-Mg Alloy Aged at Low Temperatures. *Metallurgical and*
454 *Materials Transactions A: Physical Metallurgy and Materials Science*, 48(4), 2040–
455 2050. <https://doi.org/10.1007/s11661-017-3992-2>
- 456 11. Yan, J., Heckman, N. M., Velasco, L., & Hodge, A. M. (2016). Improve sensitization and
457 corrosion resistance of an Al-Mg alloy by optimization of grain boundaries. *Scientific*
458 *Reports*, 6. <https://doi.org/10.1038/srep26870>
- 459 12. Scotto D’Antuono, D., Gaies, J., Golumbskie, W., & Taheri, M. L. (2017). Direct
460 measurement of the effect of cold rolling on β phase precipitation kinetics in 5xxx
461 series aluminum alloys. *Acta Materialia*, 123, 264–271.
462 <https://doi.org/10.1016/j.actamat.2016.10.060>
- 463 13. Desai Choundraj, J., & Kacher, J. (2022). Influence of misorientation angle and local
464 dislocation density on β -phase distribution in Al 5xxx alloys. *Scientific Reports*, 12(1),
465 1–8. <https://doi.org/10.1038/s41598-022-05948-8>
- 466 14. Picu, R. C., & Zhang, D. (2004). Atomistic study of pipe diffusion in Al-Mg alloys. *Acta*
467 *Materialia*, 52(1), 161–171. <https://doi.org/10.1016/j.actamat.2003.09.002>

- 468 15. Birbilis, N., & Buchheit, R. G. (2005). Electrochemical Characteristics of Intermetallic
469 Phases in Aluminum Alloys. *Journal of The Electrochemical Society*, 152(4), B140.
470 <https://doi.org/10.1149/1.1869984>
- 471 16. Wu, C. T., Lee, S. L., Chen, Y. F., Bor, H. Y., & Liu, K. H. (2020). Effects of Mn, Zn
472 additions and cooling rate on mechanical and corrosion properties of Al-4.6Mg casting
473 alloys. *Materials*, 13(8). <https://doi.org/10.3390/MA13081983>
- 474 17. Zhang, R., Gupta, R. K., Davies, C. H. J., Hodge, A. M., Tort, M., Xia, K., & Birbilis, N.
475 (2016). The influence of grain size and grain orientation on sensitization in AA5083.
476 *Corrosion*, 72(2), 160–168. <https://doi.org/10.5006/1703>
- 477 18. Wen, W., Zhao, Y., & Morris, J. G. (2005). The effect of Mg precipitation on the
478 mechanical properties of 5xxx aluminum alloys. *Materials Science and Engineering A*,
479 392(1–2), 136–144. <https://doi.org/10.1016/j.msea.2004.09.059>
- 480 19. Dorin, T., Ramajayam, M., Vahid, A., & Langan, T. (2018). Aluminium Scandium Alloys.
481 In *Fundamentals of Aluminium Metallurgy* (pp. 439–494).
482 <https://doi.org/10.1016/b978-0-08-102063-0.00012-6>
- 483 20. Zhang, J. Y., Gao, Y. H., Yang, C., Zhang, P., Kuang, J., Liu, G., & Sun, J. (2020, June 1).
484 Microalloying Al alloys with Sc: a review. *Rare Metals*. University of Science and
485 Technology Beijing. <https://doi.org/10.1007/s12598-020-01433-1>
- 486 21. Li, M. jia, Liu, S., Wang, X. dong, Shi, Y. jia, Pan, Q. lin, Zhou, X. jie, ... Birbilis, N. (2022).
487 Improved intergranular corrosion resistance of Al-Mg-Mn alloys with Sc and Zr
488 additions. *Micron*, 154, 103202. <https://doi.org/10.1016/j.micron.2021.103202>
- 489 22. Filatov, Y. A., Yelagin, V. I., & Zakharov, V. V. (2000). New Al-Mg-Sc alloys. *Materials*
490 *Science and Engineering A*, 280(1), 97–101. [https://doi.org/10.1016/S0921-](https://doi.org/10.1016/S0921-5093(99)00673-5)
491 [5093\(99\)00673-5](https://doi.org/10.1016/S0921-5093(99)00673-5)
- 492 23. Tang, Z., Jiang, F., Long, M., Jiang, J., Liu, H., & Tong, M. (2020). Effect of annealing
493 temperature on microstructure, mechanical properties and corrosion behavior of Al-
494 Mg-Mn-Sc-Zr alloy. *Applied Surface Science*, 514.
495 <https://doi.org/10.1016/j.apsusc.2020.146081>
- 496 24. Kendig, K. L., & Miracle, D. B. (2002). Strengthening mechanisms of an Al-Mg-Sc-Zr
497 alloy. *Acta Materialia*, 50(16), 4165–4175. [https://doi.org/10.1016/S1359-](https://doi.org/10.1016/S1359-6454(02)00258-6)
498 [6454\(02\)00258-6](https://doi.org/10.1016/S1359-6454(02)00258-6)
- 499 25. Deng, Y., Xu, G., Yin, Z., Lei, X., & Huang, J. (2013). Effects of Sc and Zr microalloying
500 additions on the recrystallization texture and mechanism of Al–Zn–Mg alloys. *Journal*
501 *of Alloys and Compounds*, 580, 412–426.
502 <https://doi.org/10.1016/j.jallcom.2013.06.020>
- 503 26. Braun, R. (2005). Effect of thermal exposure on the microstructure, tensile properties
504 and the corrosion behaviour of 6061 aluminium alloy sheet. *Materials and Corrosion*,
505 56(3), 159–165. <https://doi.org/10.1002/maco.200403825>
- 506 27. Nebti, S., Hamana, D., & Cizeron, G. (1995). Calorimetric study of pre-precipitation and
507 precipitation in Al-Mg alloy. *Acta Metallurgica Et Materialia*, 43(9), 3583–3588.
508 [https://doi.org/10.1016/0956-7151\(95\)00023-0](https://doi.org/10.1016/0956-7151(95)00023-0)
- 509 28. Milkereit, B., Starink, M. J., Rometsch, P. A., Schick, C., & Kessler, O. (2019). Review of
510 the quench sensitivity of aluminium alloys: Analysis of the kinetics and nature of
511 quench-induced precipitation. *Materials*, 12(24).
512 <https://doi.org/10.3390/MA12244083>
- 513 29. ISO. ISO 6507-1:2005: Metallic materials -- Vickers hardness test -- Part 1: Test
514 method. , ISO (2005). Retrieved from <https://www.iso.org/obp/ui/#iso:std:iso:6507:->

- 515 1:ed-4:v1:en
- 516 30. ASTM E8. (2014). *Standard Test Methods for Tension Testing of Metallic Materials*.
517 *ASTM International* (Vol. 16). Retrieved from [https://www.astm.org/e0008_e0008m-](https://www.astm.org/e0008_e0008m-16.html)
518 [16.html](https://www.astm.org/e0008_e0008m-16.html)
- 519 31. ASTM-G67. (2004). Standard Test Method for Determining the Susceptibility to
520 Intergranular Corrosion of 5XXX Series Aluminum Alloys by Mass Loss After Exposure
521 to Nitric Acid (NAMLT Test). *Annual Book of ASTM Standards*, 1–5.
522 <https://doi.org/10.1520/G0067-18>
- 523 32. Yin, Z., Pan, Q., Zhang, Y., & Jiang, F. (2000). Effect of minor Sc and Zr on the
524 microstructure and mechanical properties of Al–Mg based alloys. *Materials Science*
525 *and Engineering: A*, 280(1), 151–155. [https://doi.org/10.1016/S0921-5093\(99\)00682-](https://doi.org/10.1016/S0921-5093(99)00682-6)
526 [6](https://doi.org/10.1016/S0921-5093(99)00682-6)
- 527 33. Xie, J., Chen, X. P., Mei, L., Huang, G. J., & Liu, Q. (2021). Investigation of the hardening
528 behavior during recrystallization annealing in Al-Mg-Sc alloy. *Journal of Alloys and*
529 *Compounds*, 859. <https://doi.org/10.1016/j.jallcom.2020.157807>
- 530 34. Lim, M. L. C., Scully, J. R., & Kelly, R. G. (2013). Intergranular Corrosion Penetration in
531 an Al-Mg Alloy as a Function of Electrochemical and Metallurgical Conditions.
532 *CORROSION*, 69(1), 35–47. <https://doi.org/10.5006/0722>
- 533 35. Jiang, J., Jiang, F., Zhang, M., Tang, Z., & Tong, M. (2020). Al₃(Sc, Zr) precipitation in
534 deformed Al-Mg-Mn-Sc-Zr alloy: Effect of annealing temperature and dislocation
535 density. *Journal of Alloys and Compounds*, 831.
536 <https://doi.org/10.1016/j.jallcom.2020.154856>
- 537 36. Xu, P., Jiang, F., Tang, Z., Yan, N., Jiang, J., Xu, X., & Peng, Y. (2019). Coarsening of
538 Al₃Sc precipitates in Al-Mg-Sc alloys. *Journal of Alloys and Compounds*, 781, 209–215.
539 <https://doi.org/10.1016/j.jallcom.2018.12.133>
- 540 37. Mogucheva, A., Yuzbekova, D., Kaibyshev, R., Lebedkina, T., & Lebyodkin, M. (2016).
541 Effect of Grain Refinement on Jerky Flow in an Al-Mg-Sc Alloy. *Metallurgical and*
542 *Materials Transactions A*, 47(5), 2093–2106. [https://doi.org/10.1007/s11661-016-](https://doi.org/10.1007/s11661-016-3381-2)
543 [3381-2](https://doi.org/10.1007/s11661-016-3381-2)
- 544 38. Zhang, Y., Liu, J. P., Chen, S. Y., Xie, X., Liaw, P. K., Dahmen, K. A., ... Wang, Y. L. (2017).
545 Serration and noise behaviors in materials. *Progress in Materials Science*, 90, 358–460.
546 <https://doi.org/10.1016/j.pmatsci.2017.06.004>
- 547 39. Liu, J., Yao, P., Zhao, N., Shi, C., Li, H., Li, X., ... Yang, S. (2016). Effect of minor Sc and Zr
548 on recrystallization behavior and mechanical properties of novel Al-Zn-Mg-Cu alloys.
549 *Journal of Alloys and Compounds*, 657, 717–725.
550 <https://doi.org/10.1016/j.jallcom.2015.10.122>
- 551 40. Ding, Y., Gao, K., Huang, H., Wen, S., Wu, X., Nie, Z., ... Zhou, D. (2019). Nucleation and
552 evolution of β phase and corresponding intergranular corrosion transition at 100–
553 230 °C in 5083 alloy containing Er and Zr. *Materials & Design*, 174, 107778.
554 <https://doi.org/10.1016/J.MATDES.2019.107778>
- 555 41. Zhu, Y., Cullen, D. A., Kar, S., Free, M. L., & Allard, L. F. (2012). Evaluation of Al₃Mg₂
556 precipitates and Mn-rich phase in aluminum-magnesium alloy based on scanning
557 transmission electron microscopy imaging. *Metallurgical and Materials Transactions*
558 *A: Physical Metallurgy and Materials Science*, 43(13), 4933–4939.
559 <https://doi.org/10.1007/s11661-012-1354-7>
- 560 42. Yan, J., & Hodge, A. M. (2017). Study of β precipitation and layer structure formation
561 in Al 5083: The role of dispersoids and grain boundaries. *Journal of Alloys and*

562 *Compounds*, 703, 242–250. <https://doi.org/10.1016/j.jallcom.2017.01.360>
563 43. Porter, D. A., Easterling, K. E., & Sherif, M. Y. (2021). *Phase Transformations in Metals*
564 and Alloys (pp. 297–299). Boca Raton: CRC Press.
565 <https://doi.org/10.1201/9781003011804>
566



Click here to access/download
Supplementary Material
Supplementary_revised_final.docx

